Adiabatic shear banding in FCC metallic single and poly-crystals using a micromorphic crystal plasticity approach

Vikram Phalke, Samuel Forest, Hyung-Jun Chang, Arjen Roos

To cite this version:

Vikram Phalke, Samuel Forest, Hyung-Jun Chang, Arjen Roos. Adiabatic shear banding in FCC metallic single and poly-crystals using a micromorphic crystal plasticity approach. Mechanics of Materials, 2022, pp.104288. 10.1016/j.mechmat.2022.104288 . hal-03627107

HAL Id: hal-03627107
https://hal.science/hal-03627107

Submitted on 1 Apr 2022

Adiabatic shear banding in FCC metallic single and poly-crystals using a micromorphic crystal plasticity approach

Vikram Phalke[a,b], Samuel Forest[a], Hyung-Jun Chang[b], Arjen Roos[b]

[a]*MINES ParisTech, PSL University, MAT – Centre des matériaux, CNRS UMR 7633, BP 87 91003 Evry, France*
[b]*Safran Tech, Rue des Jeunes Bois, Châteaufort, 78772, Magny-Les-Hameaux, France*

Abstract

Finite element (FE) simulations are performed for hat-shaped specimens made of face-centered cubic (FCC) metallic single and poly–crystals in order to investigate strain localization phenomena under adiabatic conditions which are related to adiabatic shear band (ASB) formation process. A micromorphic crystal plasticity model is used to overcome the main limitation of classical plasticity models, namely the mesh size dependency in strain localization problems. A thermodynamically consistent formulation of the constitutive equations is proposed for micromorphic thermo-elasto-viscoplasticity of single crystals. The temperature evolution under *adiabatic* conditions is derived from the competition between plastic power and energy storage. The micromorphic crystal plasticity model is used first to simulate strain localization induced by thermal softening in a metallic single crystal strip loaded in simple shear undergoing single-slip. The FE solution of this boundary-value problem is validated using an analytical solution. Regarding single crystal hat-shaped specimen simulations, five different crystal orientations are considered to study the formation, intensity and orientation of shear bands. In particular, one special crystal orientation is found resistant to shear banding. In addition, the formation of shear bands in hat-shaped polycrystalline aggregates is investigated. The specimens are polycrystalline aggregates with different grain sizes, namely the *coarse-grained* and *fine-grained* specimens with random crystal orientation distribution. Furthermore, several realizations of the microstructures are taken into account for statistical considerations. The micromorphic crystal plasticity model incorporates a characteristic length scale, which induces a grain size effect in the simulation of polycrystalline specimens. The grain boundaries act as obstacles against shear band formation. A significant grain size effect, namely *the finer the grain size the higher the resulting load*, is predicted by the simulations under *isothermal* conditions. However, the fine-grained specimens are found to fail earlier by shear banding than some coarse–grained samples, the latter being associated with significant dispersion of the results depending on grain orientations. The effect of grain size on the width of the shear band is also analyzed. The temperature-dependent material parameters and shear band widths considered in the paper correspond to Nickel-based superalloy Inconel 718 in a large temperature range. No strain hardening was considered in the hat–shaped specimen test to simplify the interpretation of the results.

Keywords: Adiabatic shear band; Single crystals; Polycrystals; Gradient crystal plasticity; Micromorphic crystal plasticity; Strain localization; Grain size effect

---

Contents

1. Introduction

The ASB formation process originates from the rapid increase of local temperature due to plastic work dissipation under high strain rate loading conditions. This, in turn, reduces the stress carrying capacity of the material and results in highly localized and unstable plastic deformation (Gilman, 1994; Zhu et al., 1995; Dodd and Bai, 2012). The flow stress dependency on temperature is associated with thermal softening, causing the stress to drop from its maximum point, thus leading to intense shear band formation. The formation of shear bands may not be considered as failure of ductile material, but as a precursor to the catastrophic fracture (Anand et al., 1987; Zhu et al., 1995). It influences the texture development and the material constitutive behavior (Dève and Asaro, 1989). The phenomenon of ASB formation can be observed in many industrial processes, for instance, machining and high-speed shaping, shearing, metal forming (Burns and Davies, 2002; Molinari et al., 2002; Dodd and Bai, 2012), and so forth. A vast review on the adiabatic shear localization in metallic materials at high strain rates by using experimental and computational techniques can be found in (Yan et al., 2021).

In recent years, considerable experimental research has been conducted to investigate the ASB formation in FCC metallic materials. The experimental shear tests on hat-shaped specimens using Split-Hopkinson pressure bars in compression mode are often used to study the material resistance to shear localization, for instance, in (Nemat-Nasser et al., 1998; Meyers et al., 2003; Xue et al., 2005; Xu et al., 2008). Meyers et al. (2003) studied the microstructural evolution of adiabatic shear localization in stainless steel. Experimental investigations of the effect of strain rates, heat treatments, and grain size on the ASB formation in hat-shaped polycrystalline Inconel 718 specimens using Split-Hopkinson pressure bar test can be found in (Johansson et al., 2016, 2017; Song et al., 2018). Furthermore, Song et al. (2018) observed that the aged top-hat sample with small grain size and fillet radius has the largest tendency to form a shear band compared to the solution treated Inconel 718 specimens. They observed shear bands of 10 µm width in aged Inconel 718 samples of average grain size 28 µm and $10 - 13$ µm in solution treated samples of average grain size 18 µm. DeMange et al. (2009) found that the precipitation hardened material more readily exhibits shear localization than the solution treated material in the shear deformation of top-hat samples. Moreover, in metallic materials and alloys, it was believed that only the dislocation mobility due to a rise in temperature causes the strain-softening. However, the recent studies, e.g., (Landau et al., 2016; Mourad et al., 2017; Longère, 2018) showed that the dynamic recrystallization (DRX) is also playing an essential part in strain softening.

From the computational perspective, it is well–known that finite element simulations of strain localization phenomena exhibit spurious mesh dependency, and the classical plasticity models are inadequate to solve the strain localization problems (Asaro and Rice, 1977; de Borst et al., 1993; Besson et al., 2009). The possible loss of ellipticity of the partial differential equations in strain-softening materials results in an ill-posed boundary-value problem and classically displays dependency on mesh size or density and element orientation. The loss of ellipticity of the PDE is a local condition that concerns rate-independent constitutive equations in the static case. It implies the non-positive value of the determinant of the material's acoustic tensor (Forest and Lorentz, 2004; Wcisło et al., 2018). Rate-dependence of the material behavior can improve the situation but it is not sufficient to regularize the general localization problem (Needleman, 1988). Numerical analyses of strain localization problems within the conventional continuum mechanics framework can be found in (Batra and Kim, 1991, 1992; Duszek-Perzyna and Perzyna, 1993, 1996; Perzyna and Korbel, 1996, 1998). It has been shown very early that the combination of dynamics and viscosity provides sufficient regularization, see (Loret and Prevost, 1990; Harirêche and Loret, 1992). However, this regularization method has anomalies compared to other ones, such as strain gradient models. For instance, it is more sensitive to the imperfections triggering the strain localization (Molinari and Clifton, 1987). In addition, there are necessary conditions of loading, viscosity, and numerical time discretization for the viscous terms to be effective in regularization, as demonstrated in (Wang et al., 1996; Benallal, 2008).

The shear band width dependency on mesh size can be overcome by introducing a characteristic length scale in the classical plasticity models according to (Aifantis, 1984; Needleman, 1988; Pamin, 1994; Kuroda and Tvergaard, 2006; Voyiadjis and Al-Rub, 2005; Anand et al., 2012; Wcisło and Pamin, 2017a; Vignjevic et al., 2018; Kaiser and Menzel, 2019). Strain gradient plasticity models, which include an intrinsic length scale in the constitutive framework, are often used to regularize strain localization problems, e.g., (Aifantis, 1984; Menzel and Steinmann, 2000; Abu Al-Rub and Voyiadjis, 2006; Anand et al., 2012; Ahad et al., 2014). Aifantis (1984, 1987) proposed a strain gradient theory by adding the Laplacian of a scalar measure of plastic strain in the yield function of the classical plasticity theory to solve the issues related to the width of shear bands. The characteristic length scale introduced in the gradient plasticity models can be associated with the width of the shear band as demonstrated in (Zbib and Aifantis, 1988; Chambon et al., 1998). The effect of higher-order gradients on ASB formation was investigated by Zhu et al. (1995) and more recently by Tsagrakis and Aifantis (2015); Liu et al. (2019). Two length scales, respectively associated with strain gradients and thermal conduction, were considered in the analysis. They showed that the width of the shear band scales with the square root of strain gradient coefficient in the absence of conduction and square root of the thermal conductivity in absence of strain gradient effects. The micromorphic theory proposed by Eringen (1999) relies on the second-order microdeformation tensor as an additional degree of freedom. The application of micromorphic theory for the strain localization phenomenon can be found in (Dillard et al., 2006; Anand et al., 2012; Mazière and Forest, 2015). In contrast to Eringen's full micromorphic theory, a reduced-order micromorphic crystal plasticity theory was proposed by Ling et al. (2018) involving a scalar-valued variable as the additional degree of freedom. It was used to analyze strain localization phenomena at finite deformation by Scherer et al. (2019). The mesh dependency issues in the shear localization problem can also be eliminated by the sub-grid method proposed in (Mourad et al., 2017; Jin et al., 2018) in the case dynamic loading conditions are applied to hat-shaped specimens.

The purpose of strain gradient plasticity is not solely related to its regularization properties but the aim is also to incorporate microstructural features in the crystal plasticity modeling, namely the development of Geometrically Necessary Dislocations (GND) under high strain gradients, see (Phalke et al., 2021), and the effect of grain boundaries and grain size.

As the yielding starts in a metallic material, the work done by the stresses is partly transferred to heat and partly to the reversible or irreversible microstructural changes in the material and leads to a rise in temperature locally affecting the elastic-plastic behavior of the material. Therefore, it is necessary to introduce thermodynamics into the plasticity framework (Bertram and Krawietz, 2012). Thermodynamically consistent formulations of the constitutive equations in classical plasticity models for the small strain strain can be found in (Bertram and Krawietz, 2012) and for finite strain gradient plasticity in (Forest and Sievert, 2003; Bertram, 2015). The second law of thermodynamics in the form of Clausius-Duhem inequality is used to find the necessary conditions required for the thermodynamically consistent formulation. A fully coupled thermo-plasticity model can also be found in (Simo and Miehe, 1992; Duszek-Perzyna and Perzyna, 1993; Yang et al., 2006; Ristinmaa et al., 2007). In many works in the literature (see, e.g., Osovski et al. (2013); Zhang et al. (2016); Lieou et al. (2019)), use is made of the Taylor-Quinney coefficient (Taylor and Quinney, 1934), a constant parameter related to the amount of plastic work converted into heat. A more precise thermodynamic description requires the definition of the stored energy function with appropriate internal variables and of the dissipative mechanisms. Thermo-mechanical couplings can in that way be incorporated in the heat equation.

The present work is limited to adiabatic conditions and therefore concentrates on the microstructure effects, namely anisotropy of crystal plasticity, GND development and grain size effects, on shear band path and width. In general, there is a competition between intrinsic length scales arising from plasticity and heat conduction during shear band formation. The emerging characteristic length scale due to the heat conduction has regularizing effects and contributes to the band structure, as demonstrated in (Lemonds and Needleman, 1986; Medyanik et al., 2007; Mcauliffe and Waisman, 2013; Wcisło and Pamin, 2017a,b). However, in the present work heat conduction effects are neglected. Under the strict adiabatic condition, the effect of heat conduction on the band structure can be neglected, as discussed in (Molinari and Clifton, 1987; Shawki and Clifton, 1989; Baucom and Zikry, 1999; Li et al., 2001; Zhang et al., 2016). McVeigh and Liu (2010) recently showed that the unphysical nature of strain localization could be observed in the classic continuum formulation, even under fully coupled thermal-mechanical formulation with heat conduction effects. Consideration of heat conduction effects delays the shear instability; however, the post-instability deformation still localizes in a single element. The explicit characteristic length scale due to microstructural features in strain gradient plasticity models introduces the effect of, e.g., the GND development and grain size effect in addition to the regularizing property. Regularization of ASB is not the only purpose of the present study but also the consideration of the effect of microstructural features.

Many numerical studies on adiabatic shear localization in metallic single crystals have been completed in recent years, for instance, in (Baucom and Zikry, 1999; Perzyna, 2002; Zhang et al., 2016). However, less attention has been given to the effect of crystal orientation on the shear band formation in single crystals. It is, therefore, one of the objectives of the present work to investigate the effect of various initial crystal orientations on the ASB formation in single crystals. In the present study, the ASB formation is only related to thermal softening, letting aside the effect of DRX. The applicability of the reduced-order micromorphic crystal plasticity model involving a single scalar-valued variable as a degree of freedom (Ling et al., 2018) is demonstrated for regularizing the ASB. A thermodynamically consistent formulation of the constitutive equations for the micromorphic crystal plasticity model is presented. At first, an analytical reference solution is developed in the case of a periodic strip loaded in simple shear undergoing single-slip with linear strain and thermal softening. The FE solution of the same boundary-value problem is validated using an analytical solution initially developed for the rate-independent *isothermal* case. The temperature-dependent material parameters and shear band widths considered in the paper correspond to Nickel-based super-alloy Inconel 718 in a large temperature range. Furthermore, simulations are performed with the single crystals hat-shaped specimens with different initial crystal orientations.

The second original objective of the present work is to study the transition of ASB formation from single to polycrystals. To this end, the micromorphic approach is applied to polycrystalline hat-shaped specimens simulations to predict the role of grain boundaries as obstacles to ASB, the orientation dependency, and the influence of grain size on the width of the ASB.

The outline of the paper is as follows: In section 2, the constitutive framework of thermo-elasto-viscoplastic single crystal plasticity and the thermodynamically consistent formulation of micromorphic crystal plasticity model are presented. Section 3 is dedicated to the validation of the numerical solution for a periodic strip loaded in simple shear undergoing single-slip with linear thermal softening based on the analytical solution developed for the rate-independent case. Section 4 reports on the simulations of single crystals hat-shaped specimens under static loading conditions. In section 5, the micromorphic crystal plasticity model is used to investigate ASB formation in polycrystalline hat-shaped specimens. Concluding remarks follow in section 6.

The following notations are employed in this contribution: Underlined $\underline{\boldsymbol{A}}$ and under-waved bold $\underset{\sim}{\boldsymbol{A}}$ characters are used to denote first-order and second-order tensors, respectively. The transpose, inverse and time derivative are represented as $\underset{\sim}{\boldsymbol{A}}^T$, $\underset{\sim}{\boldsymbol{A}}^{-1}$ and $\dot{\underset{\sim}{\boldsymbol{A}}}$. Simple and double contractions are understood in the sense $\underline{\boldsymbol{a}} \cdot \underline{\boldsymbol{b}} = a_i b_j$ and $\underset{\sim}{\boldsymbol{A}} : \underset{\sim}{\boldsymbol{B}} = A_{ij} B_{ij}$. Moreover, following tensor products are used: $\underline{\boldsymbol{a}} \otimes \underline{\boldsymbol{b}} = a_i b_j \underline{\boldsymbol{e}}_i \otimes \underline{\boldsymbol{e}}_j$ and $\underset{\sim}{\boldsymbol{A}} \otimes \underset{\sim}{\boldsymbol{B}} = A_{ij} B_{kl} \underline{\boldsymbol{e}}_i \otimes \underline{\boldsymbol{e}}_j \otimes \underline{\boldsymbol{e}}_k \otimes \underline{\boldsymbol{e}}_l$. Nabla operators are defined with respect to Lagrange coordinates, ∇_X, and with respect to Euler coordinates, ∇.

2. Theoretical formulation

2.1. Thermo-elasto-viscoplasticity of single crystals at finite deformation

2.1.1. Kinematics and visco-plastic flow rule

In the present work, a large deformation framework of thermo-plasticity is adopted, based on the multiplicative decomposition of total deformation gradient $\underset{\sim}{\boldsymbol{F}}$ into a recoverable thermo-elastic part $\underset{\sim}{\boldsymbol{F}}^{the}$ and a plastic part $\underset{\sim}{\boldsymbol{F}}^{p}$ combining concepts put forward by (Bertram, 2003; Ristinmaa et al., 2007):

$$\underset{\sim}{\boldsymbol{F}} = \underset{\sim}{\boldsymbol{F}}^{the} \cdot \underset{\sim}{\boldsymbol{F}}^{p}. \tag{1}$$

The spatial and the plastic velocity gradients are defined as

$$\underset{\sim}{\boldsymbol{l}} = \dot{\underset{\sim}{\boldsymbol{F}}} \cdot \underset{\sim}{\boldsymbol{F}}^{-1}, \quad \underset{\sim}{\boldsymbol{L}}^{p} = \dot{\underset{\sim}{\boldsymbol{F}}}^{p} \cdot \underset{\sim}{\boldsymbol{F}}^{p-1}. \tag{2}$$

The volume mass densities with respect to the reference configuration, the intermediate configuration, and the current configuration are ρ_0, $\rho_{\#}$ and ρ, respectively, given by

$$J = \det(\underset{\sim}{\boldsymbol{F}}) = \frac{\rho_0}{\rho}, \quad J^{the} = \det(\underset{\sim}{\boldsymbol{F}}^{the}) = \frac{\rho_{\#}}{\rho}, \quad J^{p} = \det(\underset{\sim}{\boldsymbol{F}}^{p}) = \frac{\rho_0}{\rho_{\#}}. \tag{3}$$

It is assumed that plastic flow is isochoric such that

$$J^{p} = \det \underset{\sim}{\boldsymbol{F}}^{p} = 1, \quad J^{the} = \det \underset{\sim}{\boldsymbol{F}}^{the} = J = \det \underset{\sim}{\boldsymbol{F}}. \tag{4}$$

Crystal plasticity in dense metals is incompressible so that $J^p = 1$. However, J^p can be different from one in the case of compressible plasticity. This situation was studied for ductile fracture of porous single crystals in (Ling et al., 2016). Moreover, the thermo-elastic strain tensor $\underset{\sim}{\boldsymbol{E}}^{the}$ is introduced as follows:

$$\underset{\sim}{\boldsymbol{E}}^{the} = \frac{1}{2}[(\underset{\sim}{\boldsymbol{F}}^{the})^{T} \cdot (\underset{\sim}{\boldsymbol{F}}^{the}) - \underset{\sim}{\boldsymbol{1}}], \tag{5}$$

with $\underset{\sim}{\boldsymbol{1}}$ denoting the second order identity tensor.

The plastic shearing rate $\dot{\gamma}^r$ on each slip system r is given by the visco-plastic flow rule proposed by Méric et al. (1991) in terms of viscosity parameters K and n,

$$\dot{\gamma}^{r} = \left\langle \frac{|\tau^{r}| - \tau_c^{r}}{K} \right\rangle^{n} \mathrm{sign}(\tau^{r}), \tag{6}$$

where Macauley brackets $< \bullet >$ denote the positive part of $\bullet$. The resolved shear stress τ^r on slip system r in a single crystal is given by

$$\tau^{r} = \underset{\sim}{\boldsymbol{\Pi}}^{M} : (\underline{\boldsymbol{m}}^{r} \otimes \underline{\boldsymbol{n}}^{r}), \tag{7}$$

where $\underline{\boldsymbol{m}}^{r}$ is the slip direction and $\underline{\boldsymbol{n}}^{r}$ is the normal to the slip plane for the slip system number r. The Mandel stress tensor $\underset{\sim}{\boldsymbol{\Pi}}^{M}$ with respect to the intermediate configuration is related to the Cauchy stress tensor $\underset{\sim}{\boldsymbol{\sigma}}$ by $\underset{\sim}{\boldsymbol{\Pi}}^{M} = J^{the}(\underset{\sim}{\boldsymbol{F}}^{the})^{T} \cdot \underset{\sim}{\boldsymbol{\sigma}} \cdot (\underset{\sim}{\boldsymbol{F}}^{the})^{-T}$. In addition, the cumulative plastic strain γ_{cum} is introduced as follows:

$$\gamma_{cum} = \int_0^t \sum_{r=1}^{N} |\dot{\gamma}^{r}| dt. \tag{8}$$

The plastic deformation rate is the result of slip processes with respect to all N slip systems and defined in the intermediate configuration as

$$\underset{\sim}{\boldsymbol{L}}^{p} = \sum_{r=1}^{N} \dot{\gamma}^{r} (\underline{\boldsymbol{m}}^{r} \otimes \underline{\boldsymbol{n}}^{r}). \tag{9}$$

2.1.2. Thermodynamic formulation

The general equations of continuum thermodynamics can be found in Appendix A. The stress power term in Clausius-Duhem inequality (Eq. A.5) is given by

$$J\underset{\sim}{\boldsymbol{\sigma}} : \underset{\sim}{\boldsymbol{D}} = J^p \underset{\sim}{\boldsymbol{\Pi}}^e : \dot{\underset{\sim}{\boldsymbol{E}}}^{the} + J^p \underset{\sim}{\boldsymbol{\Pi}}^M : \underset{\sim}{\boldsymbol{L}}^p, \tag{10}$$

with $\underset{\sim}{\boldsymbol{\Pi}}^e$ the Piola stress tensor, also called second Piola–Kirchhoff stress tensor, defined with respect to the intermediate configuration by $\underset{\sim}{\boldsymbol{\Pi}}^e = J^{the}(\underset{\sim}{\boldsymbol{F}}^{the})^{-1} \cdot \underset{\sim}{\boldsymbol{\sigma}} \cdot (\underset{\sim}{\boldsymbol{F}}^{the})^{-T}$.

The dissipation rate in the Clausius-Duhem inequality consists of mechanical and thermal dissipation rates. The mechanical dissipation rate is given by

$$\Delta_m = J\underset{\sim}{\boldsymbol{\sigma}} : \underset{\sim}{\boldsymbol{D}} - \rho_0(\dot{\Psi} + \eta\dot{T}), \tag{11}$$

and the thermal dissipation by

$$\Delta_{th} = -\underline{\boldsymbol{Q}} \cdot \frac{\nabla_X T}{T}. \tag{12}$$

The quadratic form of the free energy familiar from the thermo-elasticity is assumed to be a function of the thermo-elastic strain tensor $\underset{\sim}{\boldsymbol{E}}^{the}$, the temperature T and the internal hardening variables ζ as follows:

$$\rho_0\Psi(\underset{\sim}{\boldsymbol{E}}^{the}, T, \zeta) = \frac{1}{2} J^p \underset{\sim}{\boldsymbol{E}}^{the} : \underset{\approx}{\boldsymbol{\Lambda}} : \underset{\sim}{\boldsymbol{E}}^{the} + \rho_0 C_\varepsilon \Big[(T - T_0) - T \log\left(\frac{T}{T_0}\right)\Big] + (T - T_0)\underset{\sim}{\boldsymbol{P}} : \underset{\sim}{\boldsymbol{E}}^{the} + \rho_0\Psi_\zeta(\zeta), \tag{13}$$

where $\underset{\approx}{\boldsymbol{\Lambda}}$ is the fourth-order tensor of elastic moduli, T_0 is a reference temperature, C_ε is the specific heat of the material and $\underset{\sim}{\boldsymbol{P}}$ is a constant symmetric thermal stress tensor.

Expanding the time derivative of the free energy density function gives

$$\left(J^p \underset{\sim}{\boldsymbol{\Pi}}^e - \rho_0 \frac{\partial \Psi(\underset{\sim}{\boldsymbol{E}}^{the}, T)}{\partial \underset{\sim}{\boldsymbol{E}}^{the}}\right) : \dot{\underset{\sim}{\boldsymbol{E}}}^{the} + J^p \underset{\sim}{\boldsymbol{\Pi}}^M : \underset{\sim}{\boldsymbol{L}}^p - \rho_0\left(\eta + \frac{\partial \Psi}{\partial T}\right)\dot{T} - \rho_0 \frac{\partial \Psi}{\partial \zeta}\dot{\zeta} - \underline{\boldsymbol{Q}} \cdot \frac{\nabla_X T}{T} \geq 0, \tag{14}$$

The following state laws are adopted:

$$\underset{\sim}{\boldsymbol{\Pi}}^e = \rho_\# \frac{\partial \Psi(\underset{\sim}{\boldsymbol{E}}^{the}, T)}{\partial \underset{\sim}{\boldsymbol{E}}^{the}}, \quad \eta = -\frac{\partial \Psi}{\partial T}, \quad X = \rho_0 \frac{\partial \Psi}{\partial \zeta}, \tag{15}$$

where X is the thermodynamic force associated with the internal variable ζ. Based on the potential (13) the thermoelastic relation for the Piola stress tensor is obtained as

$$\underset{\sim}{\boldsymbol{\Pi}}^e = \underset{\approx}{\boldsymbol{\Lambda}} : \underset{\sim}{\boldsymbol{E}}^{the} - \underset{\sim}{\boldsymbol{P}}(T - T_0) = \underset{\approx}{\boldsymbol{\Lambda}} : (\underset{\sim}{\boldsymbol{E}}^{the} - \underset{\approx}{\boldsymbol{\Lambda}}^{-1} : \underset{\sim}{\boldsymbol{P}}(T - T_0)) = \underset{\approx}{\boldsymbol{\Lambda}} : (\underset{\sim}{\boldsymbol{E}}^{the} - \underset{\sim}{\boldsymbol{E}}^{th}), \tag{16}$$

and the thermal strain tensor $\underset{\sim}{\boldsymbol{E}}^{th}$ is defined as

$$\underset{\sim}{\boldsymbol{E}}^{th} = (T - T_0)\underset{\approx}{\boldsymbol{\Lambda}}^{-1} : \underset{\sim}{\boldsymbol{P}} = (T - T_0)\alpha\underset{\sim}{\boldsymbol{1}}, \tag{17}$$

which involves the thermal expansion coefficient α in the case of isotropic or cubic thermoelasticity.

2.2. Reduced-order micromorphic crystal plasticity model

In micromorphic approaches, the variables which perform the targeted strain gradient effects are selected from the available state variables, which can be a tensor of any rank (Forest, 2009, 2016). In this section, a reduced-order micromorphic approach involving a micromorphic scalar variable proposed by Ling et al. (2018) is summarized. The coupled thermo-mechanical form of the free energy density function for the micromorphic crystal plasticity is inspired by the work of (Russo et al., 2020) introduced for the Cosserat medium.

Each material point is defined by its position vector $\underline{\boldsymbol{X}}$ in the reference configuration Ω^0 and its position vector $\underline{\boldsymbol{x}}$ in the current configuration Ω^t. Two types of degrees of freedom, respectively, the displacement vector $\underline{\boldsymbol{u}}$ and the scalar microslip variable γ_χ, are applied to the material point. The scalar variable associated with the micromorphic variable γ_χ is the cumulative plastic strain γ_{cum}, cf. Eq. (8). In the present reduced-order micromorphic crystal plasticity approach, the set of degrees of freedom (DOFs) is therefore

$$\text{DOFs} = \{\underline{\boldsymbol{u}}\,, \gamma_\chi\}. \tag{18}$$

The gradients of the degrees of freedom with respect to the reference configuration are denoted by

$$\underset{\sim}{\boldsymbol{H}} = \frac{\partial \underline{\boldsymbol{u}}}{\partial \underline{\boldsymbol{X}}} = \operatorname{Grad} \underline{\boldsymbol{u}}\,, \quad \underline{\boldsymbol{K}} = \frac{\partial \gamma_\chi}{\partial \underline{\boldsymbol{X}}} = \operatorname{Grad} \gamma_\chi. \tag{19}$$

The balance equations and boundary conditions for the considered micromorphic continuum are expressed with respect to the reference configuration, in the absence of body and inertial forces, as

$$\operatorname{Div} \underset{\sim}{\boldsymbol{P}} = \underline{\boldsymbol{0}} \quad \text{and} \quad \operatorname{Div} \underline{\boldsymbol{M}} - S = 0, \quad \forall \underline{\boldsymbol{X}} \subset \Omega^0, \tag{20}$$

$$\underline{\boldsymbol{T}} = \underset{\sim}{\boldsymbol{P}} \cdot \underline{\boldsymbol{n}}_0 \quad \text{and} \quad M = \underline{\boldsymbol{M}} \cdot \underline{\boldsymbol{n}}_0, \quad \forall \underline{\boldsymbol{X}} \subset \partial\Omega^0, \tag{21}$$

with $\underset{\sim}{\boldsymbol{P}}$ being the first Piola-Kirchhoff or Boussinesq stress tensor, $\underline{\boldsymbol{T}}$ is the surface traction vector, S and $\underline{\boldsymbol{M}}$ are the generalized stresses conjugate to the micromorphic variable and its gradient, defined with respect to the reference configuration and $\underline{\boldsymbol{n}}_0$ is the outer unit normal vector to the surface element along the boundary $\partial\Omega^0$.

The cumulative plastic strain γ_{cum} is related to the microslip variable γ_χ via the relative plastic strain e_p as follows:

$$e_p := \gamma_{cum} - \gamma_\chi. \tag{22}$$

Moreover, the material under consideration is assumed to be characterized by the coupled thermo-mechanical Helmholtz free energy density function defined in terms of the thermo-elastic strain tensor $\underset{\sim}{\boldsymbol{E}}^{the}$, the relative plastic strain e_p, the gradient of the microslip variable $\underline{\boldsymbol{K}}$, temperature T and the internal hardening variable ζ as follows:

$$\Psi(\underset{\sim}{\boldsymbol{E}}^{the}, e_p, \underline{\boldsymbol{K}}, T, \zeta). \tag{23}$$

It is assumed that the Helmholtz free energy density function takes the form:

$$\begin{aligned}\rho_0\Psi(\underset{\sim}{\boldsymbol{E}}^{the}, e_p, \underline{\boldsymbol{K}}, T, \zeta) = {} & \frac{1}{2}J^p\underset{\sim}{\boldsymbol{E}}^{the} : \underset{\approx}{\boldsymbol{\Lambda}} : \underset{\sim}{\boldsymbol{E}}^{the} + \frac{1}{2}H_\chi e_p^2 + \frac{1}{2}\underline{\boldsymbol{K}}\cdot\underset{\sim}{\boldsymbol{A}}\cdot\underline{\boldsymbol{K}} + \rho_0 C_\varepsilon\Big[(T-T_0) - T\,\log\Big(\frac{T}{T_0}\Big)\Big] \\ & + (T-T_0)\underset{\sim}{\boldsymbol{P}} : \underset{\sim}{\boldsymbol{E}}^{the} + \rho_0\Psi_\zeta(T,\zeta). \end{aligned} \tag{24}$$

Expanding the time derivative of the free energy density function leads to the following form of the Clausius–Duhem inequality

$$\begin{aligned}\left(J^p\underset{\sim}{\boldsymbol{\Pi}}^e - \rho_0\frac{\partial\Psi}{\partial\underset{\sim}{\boldsymbol{E}}^{the}}\right) : \dot{\underset{\sim}{\boldsymbol{E}}}^{the} - \left(S + \rho_0\frac{\partial\Psi}{\partial e_p}\right)\dot{e}_p + \left(\underline{\boldsymbol{M}} - \rho_0\frac{\partial\Psi}{\partial\underline{\boldsymbol{K}}}\right)\dot{\underline{\boldsymbol{K}}} + S\dot{\gamma}_{cum} + J^p\underset{\sim}{\boldsymbol{\Pi}}^M : \underset{\sim}{\boldsymbol{L}}^p \\ - \rho_0\left(\eta + \frac{\partial\Psi}{\partial T}\right)\dot{T} - \rho_0\frac{\partial\Psi}{\partial\zeta}\dot{\zeta} - \underline{\boldsymbol{Q}}\cdot\frac{\nabla_X T}{T} \geq 0.\end{aligned} \tag{25}$$

The following state laws are adopted:

$$\underset{\sim}{\boldsymbol{\Pi}}^e = \rho_\#\frac{\partial\Psi}{\partial\underset{\sim}{\boldsymbol{E}}^{the}}, \quad S = -\rho_0\frac{\partial\Psi}{\partial e_p}, \quad \underline{\boldsymbol{M}} = \rho_0\frac{\partial\Psi}{\partial\underline{\boldsymbol{K}}}, \quad \eta = -\frac{\partial\Psi}{\partial T}, \quad X = \rho_0\frac{\partial\Psi}{\partial\zeta}. \tag{26}$$

The residual dissipation rate, which restricts the material flow and hardening rules in connection with the yield condition, from Eq. (25) is given by

$$J^p\underset{\sim}{\boldsymbol{\Pi}}^M : \underset{\sim}{\boldsymbol{L}}^p + S\dot{\gamma}_{cum} - X\dot{\zeta} - \underline{\boldsymbol{Q}}\cdot\frac{\nabla_X T}{T} \geq 0. \tag{27}$$

The thermodynamic forces associated with arguments of the Helmholtz free energy function are derived from the potential (24):

$$\underset{\sim}{\boldsymbol{\Pi}}^e = \underset{\approx}{\boldsymbol{\Lambda}} : (\underset{\sim}{\boldsymbol{E}}^{the} - \underset{\sim}{\boldsymbol{E}}^{th}), \quad S = -H_\chi e_p = -H_\chi(\gamma_{cum} - \gamma_\chi), \quad \underline{\boldsymbol{M}} = \underset{\sim}{\boldsymbol{A}}\cdot\underline{\boldsymbol{K}}. \tag{28}$$

The form of the dissipation rate gives an incentive to introduce the following yield function

$$f^r = |\tau^r| + S - \tau_c^r = |\tau^r| - (\tau_c^r - S), \tag{29}$$

which can be put in the form

$$f^r = |\tau^r| - (\tau_c^r - S) = |\tau^r| - (\tau_c^r - \mathrm{Div}\,\underline{\boldsymbol{M}}) \tag{30}$$

where the balance law (20) connecting the generalized stresses has been taken into account. The generalized stress S in the previous equation is enhancing the hardening behavior and is regarded as a source of additional isotropic hardening. It is assumed that the second-order tensor $\underset{\sim}{\boldsymbol{A}} = A\underset{\sim}{\boldsymbol{1}}$, A being the generalized modulus which is assumed to be constant in space. This is the case in isotropic and cubic elasticity. The additional partial differential equation connecting γ_χ and γ_{cum} then follows from the balance equation in (20) and the state laws in (26) as

$$\gamma_\chi - \frac{A}{H_\chi}\,\triangle_X\,\gamma_\chi = \gamma_{cum}, \tag{31}$$

where $\triangle_X$ is the Laplace operator with respect to the reference configuration. When inserted in the yield function, this gives

$$f^r = |\tau^r| - (\tau_c^r - A\,\mathrm{Div}(\mathrm{Grad}\,\gamma_\chi)) = |\tau^r| - (\tau_c^r - A\,\triangle_X\,\gamma_\chi). \tag{32}$$

which shows that the enhanced hardening is connected to the Laplacian of the microslip variable.

In the micromorphic crystal plasticity model, the coupling modulus H_χ ensures that γ_{cum} and γ_χ take close values. When the coupling modulus H_χ takes a high enough value, γ_χ almost coincides with γ_{cum} ($\gamma_\chi \simeq \gamma_{cum}$) so that the micromorphic model reduces to a strict strain gradient plasticity model. The strict equality between γ_{cum} and γ_χ can be ensured by the introduction of a Lagrange multiplier instead of the penalty term H_χ, which is treated as an additional degree of freedom as demonstrated in (Scherer et al., 2020). In the present work, the penalized micromorphic model is used throughout.

2.3. Temperature evolution under adiabatic conditions

The energy balance for the micromorphic crystal plasticity model with respect to the reference configuration is written in the form

$$\rho_0 \dot{e} = J \underset{\sim}{\boldsymbol{\sigma}} : \underset{\sim}{\boldsymbol{D}} + S\dot{\gamma}_\chi + \underline{\boldsymbol{M}} \cdot \dot{\underline{\boldsymbol{K}}} + \mathcal{Q}. \tag{33}$$

The Clausius-Duhem inequality then reads

$$J \underset{\sim}{\boldsymbol{\sigma}} : \underset{\sim}{\boldsymbol{D}} + S\dot{\gamma}_\chi + \underline{\boldsymbol{M}} \cdot \dot{\underline{\boldsymbol{K}}} - \rho_0(\dot{\Psi} + \eta\dot{T}) - \underline{\boldsymbol{Q}} \cdot \frac{\nabla_X T}{T} \geq 0. \tag{34}$$

The previous equation consists of mechanical and thermal dissipation. The mechanical dissipation is given by

$$\Delta_m = J \underset{\sim}{\boldsymbol{\sigma}} : \underset{\sim}{\boldsymbol{D}} + S\dot{\gamma}_\chi + \underline{\boldsymbol{M}} \cdot \dot{\underline{\boldsymbol{K}}} - \rho_0(\dot{\Psi} + \eta\dot{T}), \tag{35}$$

and the thermal dissipation is still given by Eq. (12).
Substituting the free energy production rate obtained from Eq. (33) and (A.4) into the previous equation leads to

$$J \underset{\sim}{\boldsymbol{\sigma}} : \underset{\sim}{\boldsymbol{D}} + S\dot{\gamma}_\chi + \underline{\boldsymbol{M}} \cdot \dot{\underline{\boldsymbol{K}}} - \operatorname{div} \underline{\boldsymbol{q}} + r = \rho_0 \dot{e} = \rho_0 \left[\frac{\partial \Psi}{\partial \underset{\sim}{\boldsymbol{E}}^{the}} : \dot{\underset{\sim}{\boldsymbol{E}}}^{the} + \frac{\partial \Psi}{\partial e_p} \dot{e}_p + \frac{\partial \Psi}{\partial \underline{\boldsymbol{K}}} \cdot \dot{\underline{\boldsymbol{K}}} + \frac{\partial \Psi}{\partial T} \dot{T} + \frac{\partial \Psi}{\partial \zeta} \dot{\zeta} + \dot{T}\eta + T\dot{\eta} \right]. \tag{36}$$

Simplification of the previous equation after taking the state laws from (26) into account provides

$$J^p \underset{\sim}{\boldsymbol{\Pi}}^M : \underset{\sim}{\boldsymbol{L}}^p + S\dot{\gamma}_{cum} - \operatorname{div} \underline{\boldsymbol{q}} + r = \rho_0 \left[\frac{\partial \Psi}{\partial \zeta} \dot{\zeta} + T\dot{\eta} \right]. \tag{37}$$

The detailed derivation for the temperature evolution can be found in Appendix B. The following two simplified cases are discussed for the temperature evolution.

In this work, the thermodynamic processes are assumed to be *adiabatic* in nature, wherein there is no heat transfer to the surrounding and no external heat source present such that

$$\underline{\boldsymbol{q}} = 0, \quad r = 0. \tag{38}$$

Therefore, terms $\operatorname{div} \underline{\boldsymbol{q}}$ and r in (B.4) vanish.

Case 1: It is assumed that the contribution of the temperature dependence of the elastic constants and specific heat of the material can be neglected compared to plastic power. Also, the contributions of second order derivatives (variation of thermal stress with respect to the temperature) are considered very small compared to internal dissipation terms. Then (B.4) can be written as follows:

$$\rho C_\varepsilon \dot{T} = \underset{\sim}{\boldsymbol{\Pi}}^M : \underset{\sim}{\boldsymbol{L}}^p + S\dot{\gamma}_{cum} - X\dot{\zeta} \quad \text{with} \quad X = \rho_0 \frac{\partial \Psi}{\partial \zeta}. \tag{39}$$

In addition, in the present work, hat-shaped specimen simulations are performed in the absence of classical hardening, which means that $\tau_c^r = \tau_0$ is a constant in (29). Therefore, the contribution of internal hardening variable to the stored energy is not considered. The resulting form of temperature evolution is given in case 2.

Case 2: The two first terms in (39) denote the heat generated by the plastic power and represent the main contribution to thermo-mechanical phenomenon. It is assumed that all the plastic work done is converted into heat so that

$$\rho C_\varepsilon \dot{T} = \underset{\sim}{\boldsymbol{\Pi}}^M : \underset{\sim}{\boldsymbol{L}}^p + S\dot{\gamma}_{cum}. \tag{40}$$

3. Simple shear test with strain or thermal softening

An analytical reference solution initially developed for the rate-independent case with linear strain softening for a periodic strip loaded in simple shear undergoing single-slip in (Scherer et al., 2019) is recalled in Appendix C. The introduction of softening induces strain localization in a band of finite width characterized by the parameters of the micromorphic model. This solution will be adapted to account for thermal softening and provide a validation test for the FE implementation of the thermomechanical micromorphic model in the code.

3.1. FE solution with linear strain softening

The implementation of the isothermal micromorphic single crystal plasticity model in the finite element code Zset[1] is described in detail in Ling et al. (2018). The interpolation of displacement and microslip degrees of freedom is respectively quadratic and linear. The use of quadratic shape functions for displacement degrees of freedom limits locking effects in large deformation incompressible plasticity. However, linear shape functions are used for microslip degrees of freedom to limit the number of additional degrees of freedom. The argument is also that microslip degrees of freedom are strain-like variables that can be compared to actual strains, corresponding to first derivatives of the displacement field. In fact, the simultaneous use of quadratic interpolation for displacement and microslip is possible but remains to be investigated. The geometry considered in the FE simulations is shown in Fig. C.28. It is discretized into 400 C3D20R elements, which are 20 node reduced integration brick elements. A material defect is introduced at the center to trigger strain localization in the periodic strip, (see Fig. C.28). The defect is of one element size and assigned with an initial critical resolved shear stress 1% smaller than the matrix. The material parameters used for the FE solution are summarized in Table

---

[1] http://www.zset-software.com/

Table 1: Numerical values of material parameters used for the numerical simulation of simple shear test at the initial temperature of 923K.

C_{11}	C_{12}	C_{44}	τ_0	H	H_χ	A	λ	L
208.1 GPa	144.7 GPa	97.6 GPa	303 MPa	-45 MPa	10^3MPa	0.04N	0.073 mm	1.0 mm

1. The elasticity moduli correspond to a nickel–base superalloy at 923 K, see Abdul-Aziz and Kalluri (1991). Periodicity conditions are applied and the tensor $\underset{\sim}{\bar{\boldsymbol{F}}}$ is prescribed according to Eq. (C.1).

Fig. 1a displays the cumulative plastic strain field predicted by the micromorphic crystal plasticity model. The FE solution is validated with respect to the variation of γ_χ along X_2 direction at $\bar{F}_{12} = 0.01$ with the analytical solution given by Eq. (C.13). This comparison is shown in Fig. 1b. Perfect agreement is observed for $\bar{F}_{12} = 0.01$ and for all other values of $\bar{F}_{12}$. The analytically calculated, refer Eq. (C.11), and numerically observed width of the localization zone is measured to be 2.6λ.

3.2. FE solution with linear thermal softening

In the studied simplified problem of single-slip periodic strip undergoing simple shear, the rate of plastic work $\underset{\sim}{\boldsymbol{\Pi}}^M : \dot{\underset{\sim}{\boldsymbol{F}}}{}^p \underset{\sim}{\boldsymbol{F}}{}^{p-1} + S\dot{\gamma}_{cum}$ becomes[2] $(\tau + S)\dot{\gamma}$, which gives the temperature evolution according to (40) as

$$\dot{T} = \frac{(\tau + S)\dot{\gamma}}{\rho C_\varepsilon}. \tag{41}$$

In the rate independent limit, the yield function (29) is equal to zero under plastic loading so that $\tau + S = \tau_0$ in the absence of classical hardening. The critical resolved shear stress (CRSS) $\tau_0(T)$ is a function of temperature. An affine dependence is chosen for this analytical example

$$\tau_0 = \tau_{RT} + H_T(T - T_{RT}), \tag{42}$$

where $H_T < 0$ is the negative slope of the linear variation of τ_0 with temperature, T_{RT} is the room temperature and τ_{RT} is the CRSS value at room temperature. Then, Eq. (41) becomes

$$\dot{T} = \frac{\tau_0\dot{\gamma}}{\rho C_\varepsilon}. \tag{43}$$

In order to obtain a simple analytic solution for the temperature, τ_0 is approximated by the constant value: $\hat{\tau}_0 = \tau_{RT} + H_T(T_i - T_{RT})$ where T_i is some initial temperature value. In such conditions, the previous equation can be integrated, assuming monotonic loading, which leads to the following form of the temperature rise:

$$T = \frac{\tau_0\gamma}{\rho C_\varepsilon} + T_i \tag{44}$$

The yield condition (29), which includes the temperature dependent softening can now be written as follows:

$$f = |\tau| - (\hat{\tau}_0(1 + \frac{H_T\gamma}{\rho C_\varepsilon}) + H_\chi(\gamma - \gamma_\chi)) = 0. \tag{45}$$

---

[2] with appropriate choice of the orientation of slip direction vector $\underline{\boldsymbol{m}}$ so that $\tau > 0$.

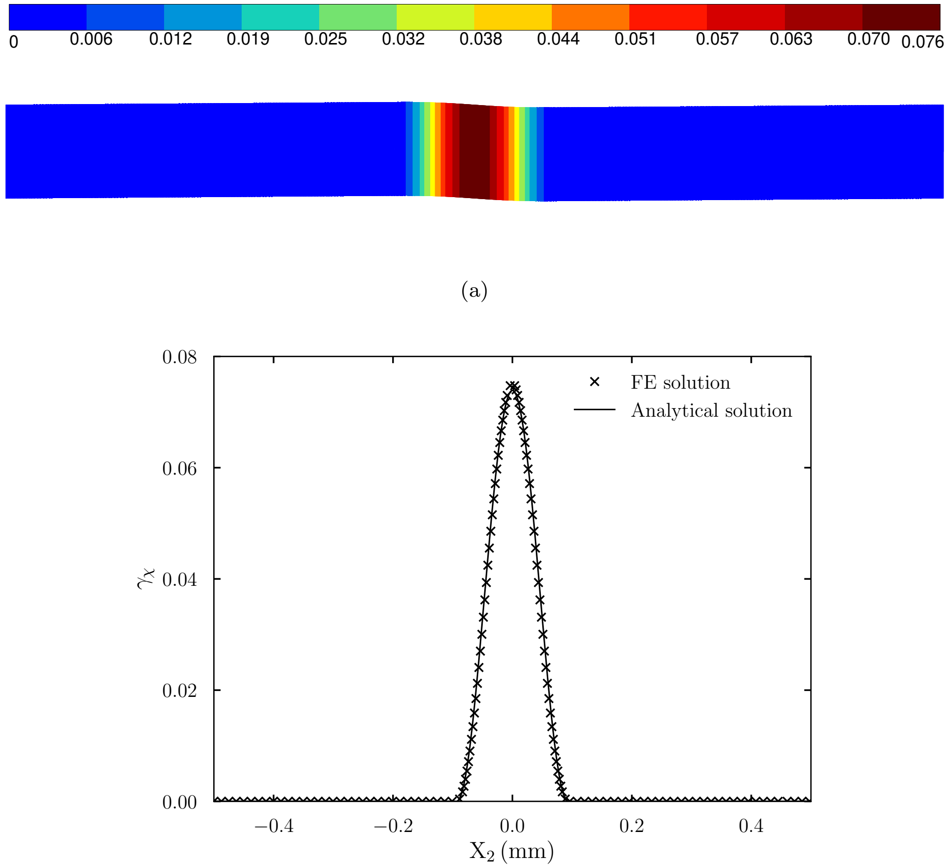

(a)

(b)

Fig. 1: (a) Contour plot of cumulative plastic strain γ_{cum} in a single-slip simple shear test with linear strain softening using the micromorphic crystal plasticity model ($H = -45$MPa, A=0.04N). (b) Comparison of FE solution with the analytical solution for the variation of γ_χ along X_2 at $\bar{F}_{12} = 0.01$.

Combining (C.8) and (45) leads to the same partial differential equation governing the microslip variable as (C.9) provided that τ_0 is replaced by $\hat{\tau}_0$ and the hardening modulus H has the following definition

$$H \equiv \frac{H_T \tau_0}{\rho C_\varepsilon}. \tag{46}$$

The solution of the PDE (C.9) still has the form (C.12) where the constants λ and κ are given by Eq. (C.11) with the new definition of H and $\tau_0 \equiv \hat{\tau}_0$.

This approximate solution is now compared to the FE prediction. For that purpose, the evolution of the temperature driven by the adiabatic condition (40) is numerically integrated in the code by means of a second order Runge-Kutta method with automatic time stepping Besson et al. (2009). The material parameters used for the FE solution with the linear thermal softening are given in Table 2. The value of H_T has been chosen so that the associated modulus given by (46) takes the same value $H = -45$ MPa as in the example of linear strain softening, see Section 3.1.

In the FE analysis, no approximation is introduced and the CRSS has the temperature dependent expression (42). The cumulative plastic strain and temperature fields predicted by the micromorphic crystal plasticity model with linear thermal softening are shown in Fig. 2a and 2b, respectively. The temperature evolution due to *adiabatic* heating is considered as in the *case 2* presented in section 2.2, cf. Eq. (40). The comparison of the FE solution for γ_χ variation with the approximate analytical solution obtained from Eq. (C.12) is displayed in Fig. 2c at $\bar{F}_{12} = 0.01$. The analytically calculated and numerically simulated width of the deformation zone is 2.6λ, which is equal to the value obtained with linear strain softening. This is due to the fact that the temperature softening modulus H_T has been chosen so that the equivalent modulus H is the same as the softening modulus used in Section 3.1. The approximation of τ_0 by $\hat{\tau}_0$ in the analytical solution does not lead to significant differences compared to the full FE solution, due to the fact that the temperature changes remain limited, see Fig. 2b. The limited heating was however sufficient to trigger plastic strain localization.

This study shows that the analytical solution initially developed for the rate-independent case for the linear strain softening can be used in the linear thermal softening case after establishing a relation between the slope of the linear variation of the CRSS with respect to temperature, H_T, and an equivalent linear strain softening modulus H. Furthermore, the FE implementation with linear strain, and thermal softening has been validated by means of this analytical solution.

4. Application to single crystals hat-shaped specimens

This section presents the application of the proposed thermo-mechanical micromorphic constitutive framework to single crystal hat-shaped specimens. The aim is to investigate the effects of initial crystal orientation on the formation and orientation of adiabatic shear bands. The material behavior considered in the simulations is elastic-perfectly plastic, and the material parameters correspond to nickel-based super-alloy Inconel 718. Furthermore, the temperature evolution due to *adiabatic* heating is considered as in the *case 2* presented in section 2.2 (Eq. (40)).

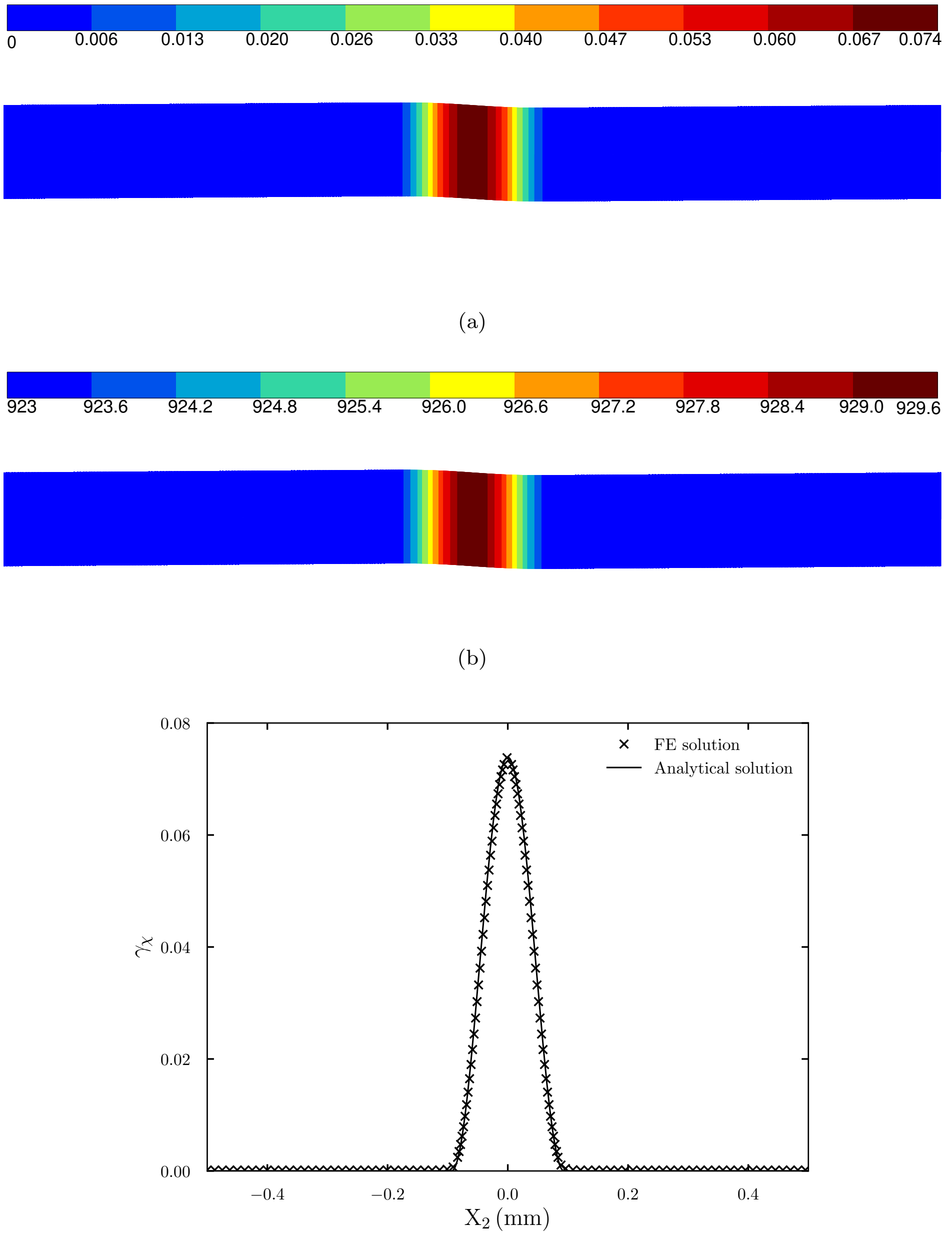

(a)

(b)

(c)

Fig. 2: Contour plots of (a) cumulative plastic strain γ_{cum}, and (b) temperature in the single-slip simple shear test with thermal softening using the micromorphic crystal plasticity model (T_i=923K, A=0.04N) subjected to *adiabatic* heating. (c) Comparison of the FE solution obtained using the micromorphic crystal plasticity model with the analytical solution for the variation of microslip variable γ_χ along X_2 at $\bar{F}_{12} = 0.01$.

Table 2: Numerical values of the material parameters used in the simulations of single-slip periodic strip undergoing simple shear with thermal softening using the micromorphic crystal plasticity model.

C_{11}	C_{12}	C_{44}	H_χ	H_T	T_{RT}
208.1 MPa	144.7 MPa	97.6 MPa	10^3MPa	-0.48MPa/K	293K
τ_{RT}	τ_{1523K}	A	T_i	ρ	C_ε
606MPa	10MPa	0.04N	923K	7.8×10^{-6}kg mm^{-3}	412 Jkg^{-1}K^{-1}

The outline of this section is as follows. The temperature-dependent material parameters of Inconel 718 are summarized in section 4.1. The criteria for the selection of gradient parameters (A and H_χ) are given in section 4.2. Then, the geometry, boundary conditions and considered crystal orientations are presented in section 4.3. In section 4.4, mesh sensitivity analysis is performed with the classical and micromorphic crystal plasticity models. Results and discussion follow in section 4.5.

4.1. Material properties of Inconel 718

The temperature-dependent material parameters considered in this paper correspond to Nickel-based superalloy Inconel 718 in a large temperature range. The characterization of high strain rate compressive loading behavior within a wide range of temperature for Inconel 718 was performed in (Iturbe et al., 2017). In this paper, the material properties investigated are in the temperature range of $294 - 1323$ K, close to those found in machining at high strain rates ($1 - 100$ s^{-1}). The stress-strain behavior of Inconel 718 in the temperature range of $294 - 1323$ K (strain rate = 1s^{-1}) and variation of the yield strength (YS) and ultimate tensile strength (UTS) with respect to the temperature are shown in Fig. 3a and Fig. 3b, respectively. In general, the flow stress of Inconel 718 increases with increasing strain rate and decreasing temperature. It can be seen from Fig. 3b that the strength of the material decreases with increasing temperature at a specified strain rate. This thermal softening behavior is not very noticeable until the temperature of 923 K.

The material parameters τ_0, K, and n are identified against the experimental stress-strain curves obtained from the work of (Iturbe et al., 2017) with simple tension tests performed on a single Gauss point using the classical crystal plasticity model presented in section 2.1. The material constants used in the numerical simulations are presented in Table 3. Moreover, the material parameters τ_0, K, and n are introduced as functions of temperature in the present simulations as given in Table 4. Linear interpolation is used for temperature values other than those listed in the table. For simplicity, elasticity moduli are taken as temperature independent since their variation is not the main driving force for shear banding. A typical value of 1550 K is considered for the melting temperature.

The thermodynamically consistent framework of the constitutive equations for the micromorphic crystal plasticity model presented in this work can predict a more realistic temperature rise in line with the experimental measurements in the case of elasto-viscoplastic material behavior. With con-

Table 3: Values of the material parameters used in the single crystalline and polycrystalline hat-shaped specimen simulations.

C_{11}	C_{12}	C_{44}	H_χ	A
208.1 MPa	144.7 MPa	97.6 MPa	10^3MPa	0.004 - 0.04 N
T_{RT}	T_i	ρ	C_ε	
293K	923K	7.8×10^{-6}kg mm^{-3}	412 Jkg^{-1}K^{-1}	

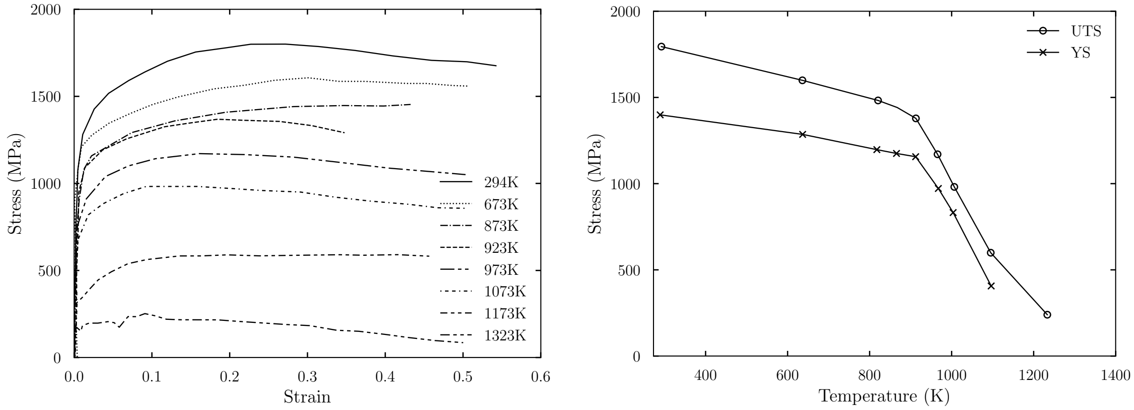

(a) (b)

Fig. 3: Influence of the temperature on (a) stress-strain behavior (b) yield strength and ultimate tensile strength of the Inconel 718 when compressed at a strain rate of 1s^{-1} (Iturbe et al., 2017).

sideration of strain-hardening, the stored energy rate term will contribute to temperature evolution under adiabatic conditions, see Eq. (39). It is common practice to assume a constant value 0.9 of the Taylor-Quinney parameter. However, in reality, its value can be less than 0.9. This framework with work-hardening will allow for evolving Taylor-Quinney parameters predicted by suitable free energy density functions. The present simulations are however limited to no-hardening crystals for the sake of simplicity. Evolution equations for dislocation densities were used in the micromorphic model by (Ling et al., 2018) and could also be considered in the hat-shaped specimen tests.

4.2. Selection of the gradient parameters A and H_χ

The characteristic length scale emerges in the development of shear bands and is related to their width. The width of the shear band is finite and set by the material microstructure. In general, this characteristic length scale differs depending on the specific localization pattern observed for the particular boundary-value problem considered. The width of the shear band exhibited by the solution of the multislip boundary-value problems is generally linked to the characteristic length scale ℓ_c defined as

$$\ell_c = \sqrt{\frac{A(H + H_\chi)}{|H| H_\chi}}, \tag{47}$$

Table 4: Temperature dependent material parameters used in the single crystalline and polycrystalline hat-shaped specimen simulations. These parameters are related to the strain rate range of 0.1 s^{-1} to 1 s^{-1}.

Temperature (K)	τ_0 (MPa)	K (MPa.$s^{1/n}$)	n
298	570	5	15
923	520	5	15
1073	340	8	10
1173	170	20	5.5
1323	61	35	4
1523	10	50	2

This definition is taken from the simple localization analysis of Appendix C and involves the coupling modulus H_χ, the higher order modulus A, and the strain softening modulus H. Moreover, the size effects in crystal plasticity occur at a scale ranging from hundreds of nanometers to a few tens of microns. This sets bounds for the values of the chosen characteristic length scale of the model. Usually, the coupling modulus H_χ is chosen large enough so that the cumulative plastic strain γ_{cum} and microslip variable γ_χ almost coincide. In that case, the micromorphic model can be regarded as an actual strain gradient plasticity model. On the other hand, the micromorphic model response saturates for smaller sizes if the chosen value of H_χ is not large enough as demonstrated for single crystal microwire torsion test simulations in (Scherer et al., 2020) and in polycrystal simulations when d_{avg} is of the order of or smaller than ℓ_c (Cordero et al., 2012). When the average grain size $d_{avg} \gg \ell_c$, strain gradient effects vanish and the deformation field predicted by the micromorphic crystal plasticity model is almost identical to that of the classical crystal plasticity model. The gradient parameter A controls the width of the shear band in strain localization problem. Based on these requirements, the gradient parameters A and H_χ are chosen such that the width of formed shear band in the single crystal simulations remains always smaller than horizontal shift of the corners which is 0.1 mm. On the other hand, the gradient parameters are such that ℓ_c is of the order of the smallest grain size to be considered in the shear region in polycrystalline simulations. Two values of the gradient parameter A, 0.004 N, and 0.04 N are chosen for the analysis which satisfy the aforementioned conditions. Moreover, the selected value of H_χ is 10^3 MPa. It has been checked to be high enough to get values of e_p sufficiently close to zero, and in the mean time small enough to avoid numerical problems associated with ill-conditioned matrices in the presence of penalty terms.

4.3. Simulation setup, slip systems, and initial crystal orientations

In the first part of the study, shear tests of single crystal hat-shaped specimens are performed to investigate the development of ASB in the post-localization regime. The shape and geometry of

Table 5: Initial crystal orientations used in the single crystal hat-shaped specimen simulations.

Crystal orientations	Short notation
[100]-[010]-[001]	[100]-[010]
$[110]$-$[001]$-$[1\bar{1}0]$	[110]-[001]
$[001]$-$[110]$-$[1\bar{1}0]$	[001]-[110]
$[\bar{1}\bar{1}2]$-$[111]$-$[1\bar{1}0]$	$[\bar{1}\bar{1}2]$-$[111]$
$[111]$-$[\bar{1}\bar{1}2]$-$[1\bar{1}0]$	$[111]$-$[\bar{1}\bar{1}2]$

the hat-shaped specimen promote shear failure even in materials which are not sensitive to shear localization (Peirs et al., 2008). A symmetric hat-shaped specimen under plane strain condition with one element along the thickness of 0.025 mm is considered for the study. In practice, axi-symmetric geometries are often used but their analysis would require too large 3D simulations in the case of polycrystals considered in the present work.

The geometry, dimensions, and the applied boundary conditions of the specimen are shown in Fig. 4. The height of the shear zone is $h = 1$ mm. The corners of the shear region are rounded with a radius of $R = 0.05$ mm. Rounded corners allow for the reduction of stress concentration and postpone strain localization (Peirs et al., 2008). Note that the geometry is such that there is an horizontal shift of 0.1 mm between the two corners, see Fig. 4. The FE mesh of this geometry is made of 20 node brick elements with reduced integration (C3D20R). The macroscopic strain rate which the specimens are subjected to in the numerical simulations is defined a $\Delta U/h\Delta t$, where ΔU is the relative displacement linearly applied during the test duration Δt. It has the value 0.1 s^{-1}.

The five different initial crystal orientations investigated in the study are given in Table 5. The crystal orientations are defined with respect to the basis frame $\underline{\boldsymbol{e}}_1\underline{\boldsymbol{e}}_2\underline{\boldsymbol{e}}_3$, with $\underline{\boldsymbol{e}}_2$ being in the direction of applied load and $\underline{\boldsymbol{e}}_3$ in the direction normal to the plane. For instance, the single crystal orientation $[100] - [010] - [001]$ is such that the axes of the specimen are

$$\underline{\boldsymbol{e}}_1 = [100] \quad \underline{\boldsymbol{e}}_2 = [010] \quad \underline{\boldsymbol{e}}_3 = [001],$$

as shown in Fig. 4. For the sake of simplicity, crystal orientations are represented only by the basis plane $\underline{\boldsymbol{e}}_1 - \underline{\boldsymbol{e}}_2$ (see Table 5) in the following sections. The definition of the octahedral slip systems in FCC lattice structure is specified in Table 6.

4.4. Mesh sensitivity analysis

Three distinct mesh discretizations in the shear region with 66720, 88560, and 135540 nodes shown in Fig. 5 are used to investigate the effect of mesh density on the normalized load–displacement curves and the shear band structure. The load and displacements are normalized by the height of

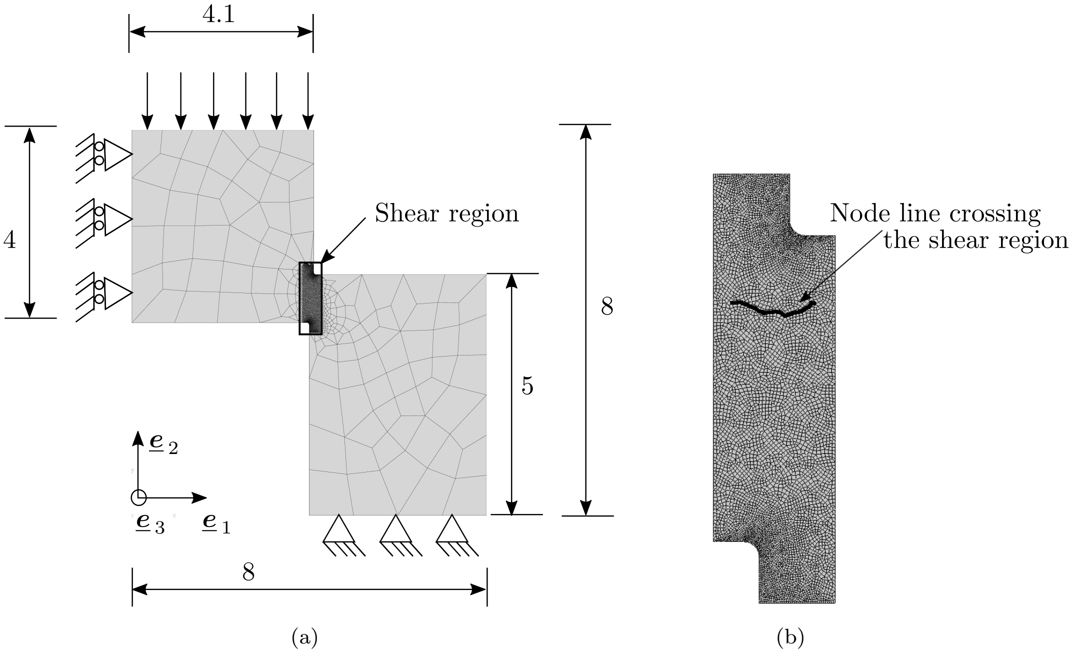

Fig. 4: Hat-shaped specimen: (a) geometry, boundary conditions and FE mesh (all dimensions are in mm). (b) Zoom at the shear region: mesh in the shear region; the black line on the figure denotes a line of nodes of the FE mesh crossing the shear region along which the cumulative plastic strain and temperature fields will be plotted.

Table 6: Definition of the octahedral slip systems in the numerical model.

Normal vector $\underline{\boldsymbol{n}}$	(111)			$(1\bar{1}1)$			$(\bar{1}11)$			$(11\bar{1})$		
Slip direction $\underline{\boldsymbol{m}}$	$[\bar{1}01]$	$[0\bar{1}1]$	$[\bar{1}10]$	$[\bar{1}01]$	$[011]$	$[110]$	$[0\bar{1}1]$	$[110]$	$[101]$	$[\bar{1}10]$	$[101]$	$[011]$
Slip system index	B_4	B_2	B_5	D_4	D_1	D_6	A_2	A_6	A_3	C_5	C_3	C_1

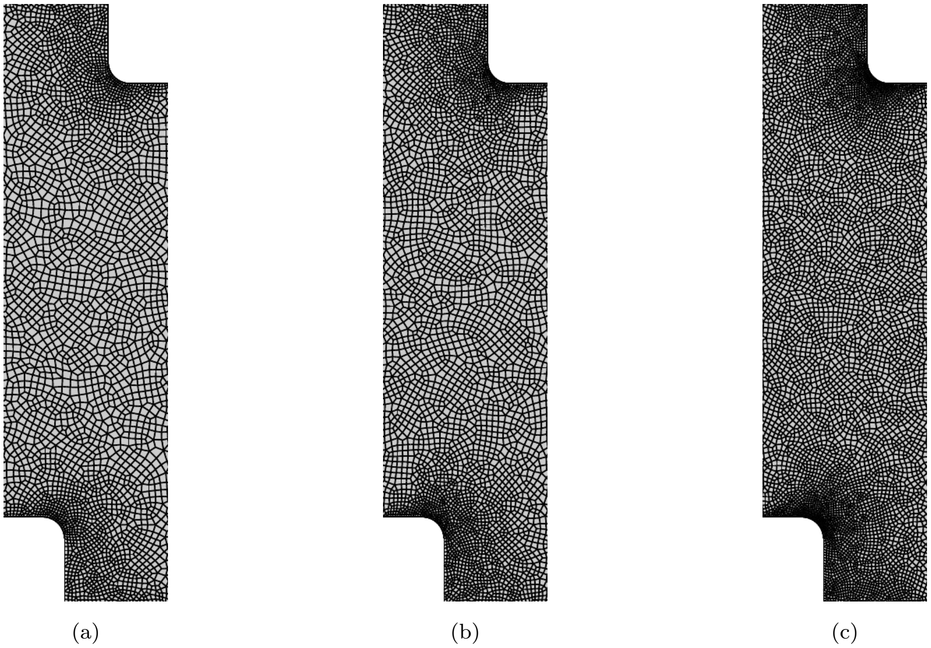

(a) (b) (c)

Fig. 5: Three discretizations in the shear region used for the mesh sensitivity analysis with (a) 66720, (b) 88560, and (c) 135540 nodes.

the shear region $h = 1$ mm. The simulations are performed with the classical and micromorphic crystal plasticity models with *adiabatic* heating for $[001]-[110]$ initial crystal orientation. The initial temperature, T_i, of the specimens is assumed to be 923 K. The limitation of the classical crystal plasticity model, namely the mesh size dependency in strain localization problems, is demonstrated by Fig. 6a. The load-displacement curves with the classical crystal plasticity model are different for the three discretizations and do not converge upon mesh refinement as demonstrated in Fig. 6a. In contrast, the load-displacement curves with the micromorphic crystal plasticity model for three discretizations are almost the same and converge upon mesh refinement as shown in Fig. 6b. The cumulative plastic strain fields and corresponding deformed geometries for the three discretizations with the classical and the micromorphic crystal plasticity models are shown in Fig. 7a and 7b, respectively. The formed shear bands width with the classical crystal plasticity model exhibits well-known pathological mesh dependency, which always collapses to one element size irrespective of the mesh size. In contrast, with the micromorphic crystal plasticity model, the width of the formed shear band is finite and independent of used spatial discretization. This suggests that the 88560 nodes in the shear region are sufficient to produce mesh-independent results. However, discretization with 135540 nodes in the shear region is used for further investigations.

4.5. Results and discussion

4.5.1. Slip system activity

The activated slip systems for different initially oriented crystals are listed in Table 7 as significant plastic deformation occurs on these slip systems. Numerically, the activated slip systems are

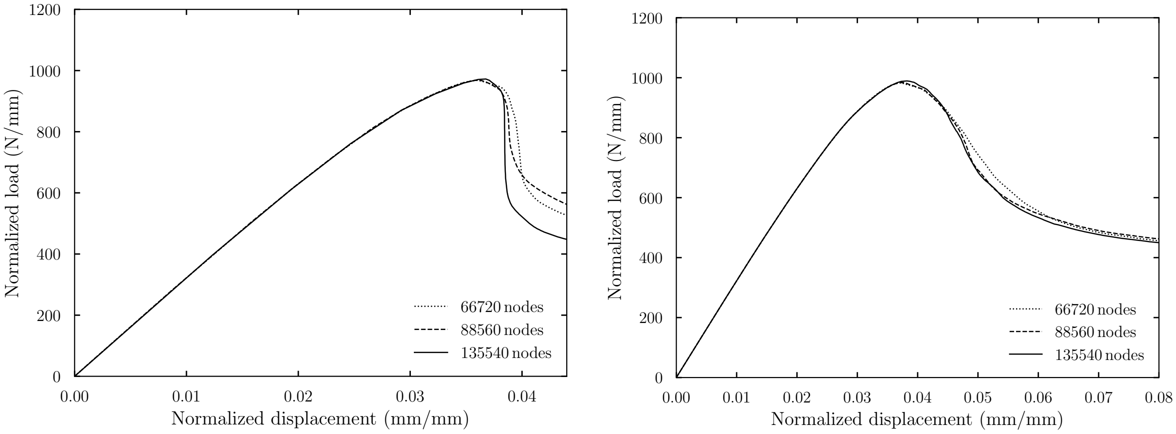

(a)

(b)

Fig. 6: Load-displacement curves for $[001]-[110]$ initially oriented crystal subjected to *adiabatic* heating (T_i =923K) for three discretizations using the (a) classical crystal plasticity model (b) micromorphic crystal plasticity model ($A =$ 0.004N).

identified when the shear band is fully formed and before the temperature within the band reaches the melting temperature. The four activated slip systems ($B4, D1, A2\,\text{and}\,C3$) for $[100]-[010]$ initially oriented crystal are neither co-planar nor co-directional to each other and show identical absolute slip rates ($|\dot{\gamma}^{B4}|$=$|\dot{\gamma}^{D1}|$=$|\dot{\gamma}^{A2}|$=$|\dot{\gamma}^{C3}|$). For $[110]-[001]$ initially oriented crystal, one pair of co-directional ($C3\,\text{and}\,C1$, $|\dot{\gamma}^{C3}|$=$|\dot{\gamma}^{C1}|$) and one pair of co-planar ($D6\,\text{and}\,A6$, $|\dot{\gamma}^{D6}|$=$|\dot{\gamma}^{A6}|$) slip systems are activated, while in $[001]-[110]$ initially oriented crystal, one pair of co-directional ($D6, A6$, $|\dot{\gamma}^{D6}|$=$|\dot{\gamma}^{A6}|$) and two pairs of co-planar ($B4, B2$ $|\dot{\gamma}^{B4}|$=$|\dot{\gamma}^{B2}|$and $C3, C1$, $|\dot{\gamma}^{C3}|$=$|\dot{\gamma}^{C1}|$) slip systems are activated. On the other hand, for both asymmetric initially oriented crystals, $[\bar{1}\bar{1}2]$-$[111]$ and $[111]$-$[\bar{1}\bar{1}2]$ activated pairs of slip system are co-planar, ($B4, B2, C3, C1$, $|\dot{\gamma}^{B4}|$=$|\dot{\gamma}^{B2}| =$ $|\dot{\gamma}^{C3}|$=$|\dot{\gamma}^{C1}|$) and ($B4, B2$, $|\dot{\gamma}^{B4}|$=$|\dot{\gamma}^{B2}|$), respectively.

4.5.2. Influence of initial crystal orientation on the shear band formation

Fig. 8 shows the load-displacement curves for five different crystal orientations. The resulting load on the hat-shaped specimen increases to its peak value, and then drops abruptly from its peak value as a consequence of thermal softening inside the bands. Furthermore, it is observed that the initiation of shear band is orientation-dependent. The normalized displacement needed for the initiation of shear band for the asymmetric crystal orientations $[\bar{1}\bar{1}2]-[111]$ and $[111]-[\bar{1}\bar{1}2]$ is lower than that for the symmetric crystal orientations $[100]-[010]$, $[001]-[110]$ and $[110]-[001]$ (see Fig. 8). The evolution of the cumulative plastic strain within shear bands at various deformation stages is shown in Fig. 9 for $[001]-[110]$ crystal orientation at the normalized displacement values of 0.04, 0.045, 0.050 and 0.055. The onset of ASB is observed at the specimen's corner at a normalized displacement of 0.04. It propagates from the corners with further increase in deformation, and the shear band is fully formed at a normalized displacement of 0.055.

The cumulative plastic strain and temperature fields in the single crystals hat-shaped specimens

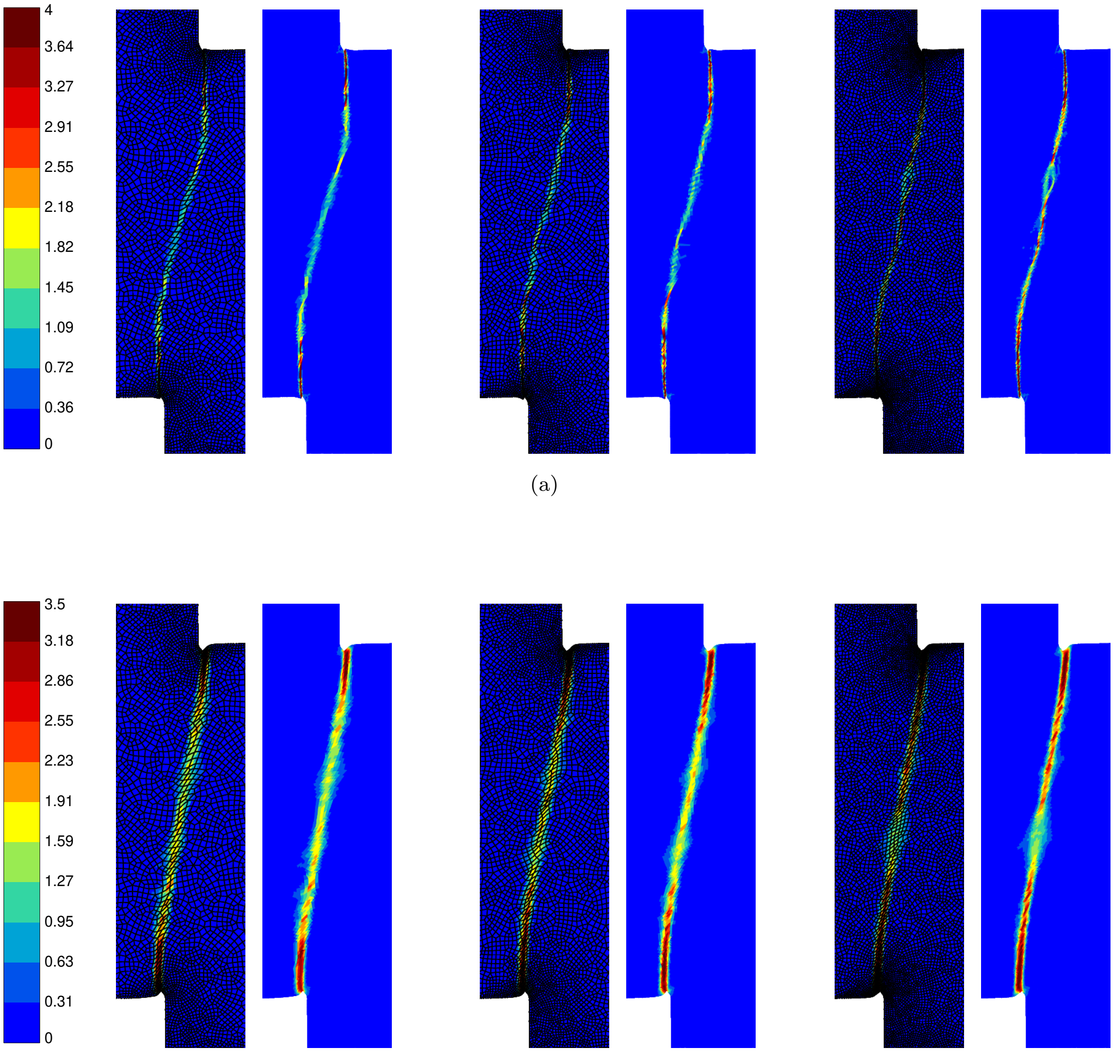

(a)

(b)

Fig. 7: Contour plots of cumulative plastic strain γ_{cum} for $[001]-[110]$ initially oriented crystal with three discretizations (66720, 88560, and 135540 nodes in the shear region) subjected to *adiabatic* heating using the (a) classical crystal plasticity model, and (b) micromorphic crystal plasticity model ($A = 0.004$N) at a normalized displacement of 0.041 mm/mm and T_i =923K, with and without showing the mesh.

Table 7: Slip systems activity inside the ASB in single crystal hat-shaped specimens.

Crystal orientations	Activated slip systems
[100]-[010]	B4,D1,A2,C3
[110]-[001]	D6,A6,C3,C1
[001]-[110]	B4,B2,D6,A6,C3,C1
[$\bar{1}\bar{1}2$]-[111]	B4,B2,C3,C1
[111]-[$\bar{1}\bar{1}2$]	B4,B2

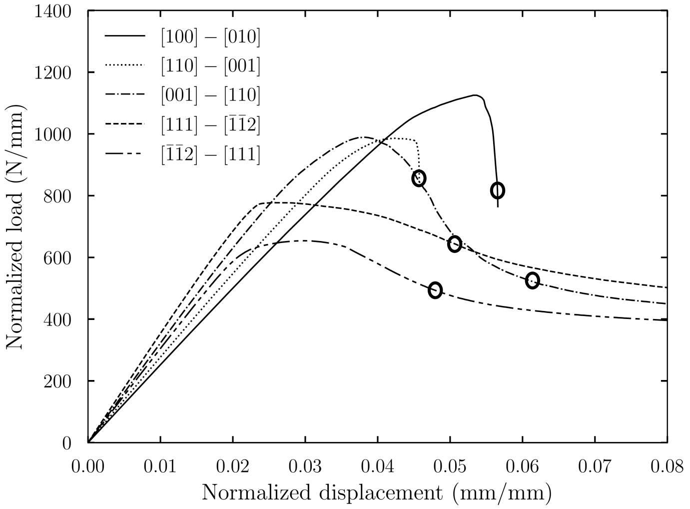

Fig. 8: Load-displacement curves for five different crystal orientations subjected to *adiabatic* heating using the micromorphic crystal plasticity model (T_i = 923K, A = 0.004N). Circles on the plot are corresponding to the normalized displacement at which cumulative plastic strain, temperature and lattice rotation fields shown next are plotted.

for five different initial crystal orientations are shown in Fig. 10 and 11, respectively. High values are observed at the corners of the specimens and lower ones at the center of the sheared region. The simulation results show that the formation and orientation of the ASB with respect to the loading axis significantly depends on the initial crystal orientation. The $[100]-[010]$ initial crystal orientation shows a stiffer response to the shear banding than the other ones. A remarkable feature is that no shear band forms connecting the corners. Instead, two parallel shear bands tend to form, oriented at an angle of about 16° clockwise with respect to the loading axis. With further straining, only one shear band remains. This band does not seem to have a crystallographic nature because the activated slip systems are neither co-planar nor co-directional. This particular situation does not favor the shear band formation. On the other hand, activated pairs of co-planar and co-directional slip systems in $[001]-[110]$, $[110]-[001]$ and $[\bar{1}\bar{1}2]-[111]$ favor the shear band formation. The initially oriented crystal $[111]-[\bar{1}\bar{1}2]$, exhibits the lowest tendency to shear band formation, and no evident shear banding is observed prior to melting temperature as it promotes less octahedral slip systems (only two slip systems are activated). On the other hand, distinct shear banding patterns are observed for the other four initially oriented crystals as it facilitates the activation of more numerous octahedral slip systems.

As the deformation becomes unstable and the shear band is fully formed, the plastic strain within the shear band increases with further deformation, but the gradient parameter A limits the width of the shear band. Fig. 12 show the γ_{cum} variation along the node line crossing the shear region of Fig. 4 when the shear band is fully formed for different initial crystal orientations. The band width w is defined as the width of the shear region surrounding the band center over which the cumulative plastic strain remains larger than 10% of the its peak value (Batra and Chen, 2001). Moreover, the observed width of the shear band is also orientation-dependent. The observed widths of the shear band from Fig. 12a in symmetric crystal orientations $[100]-[010]$, $[110]-[001]$ and $[001]-[110]$ using gradient parameter A of 0.004N are 0.05 mm, 0.075 mm and 0.08 mm, respectively. On the other hand, for both asymmetric crystal orientations $[\bar{1}\bar{1}2]-[111]$ and $[111]-[\bar{1}\bar{1}2]$ the observed width is 0.075 mm (see Fig. 12b). In addition, the predicted temperature fields and variation of temperature across the node line crossing the shear region is shown in Fig. 11 and 13. The peak temperature is observed at the center of the shear band.

4.5.3. Lattice rotation fields

Non-homogeneous plastic strain fields are usually accompanied with significant lattice rotation. The non-uniform lattice rotation in strain localization problems results in a local geometrical softening of the slip plane with which the shear band is aligned according to (Chang and Asaro, 1980; Lisiecki et al., 1982). Shear band formation is therefore possible even in work-hardening materials due to such geometric softening (Dillamore et al., 1979). Strain softening and non-homogeneous lattice rotations induce instabilities in the plastic deformation. The formation of deformation bands in crystalline materials is very often associated with lattice rotations. The lattice rotation angle ϕ can be measured

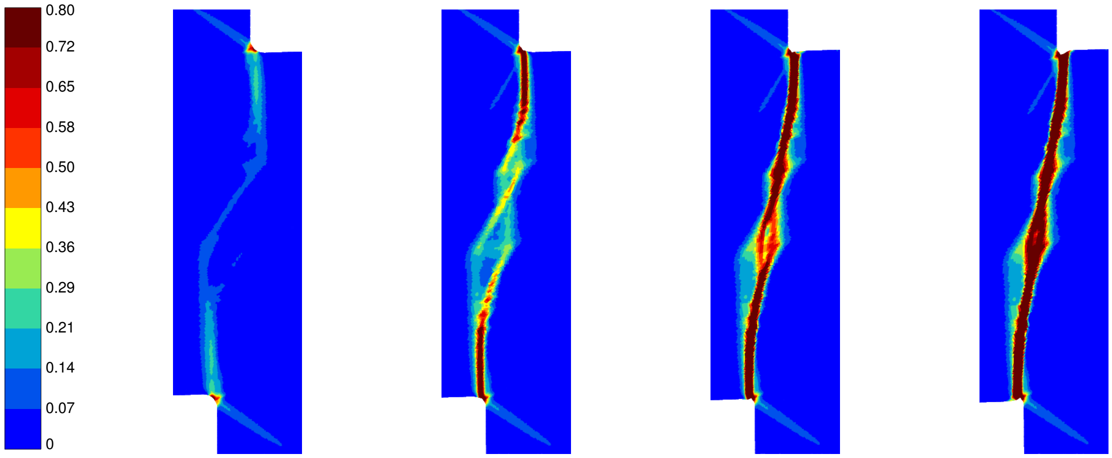

(a) (b) (c) (d)

Fig. 9: Contour plots of cumulative plastic strain at different stages showing the shear band formation with adiabatic heating using the micromorphic crystal plasticity model ([001] − [110] crystal orientation, T_i = 923K, A = 0.004N) at normalized displacements of (a) 0.04 mm/mm, (b) 0.045 mm/mm, (c) 0.050 mm/mm, and (d) 0.055 mm/mm.

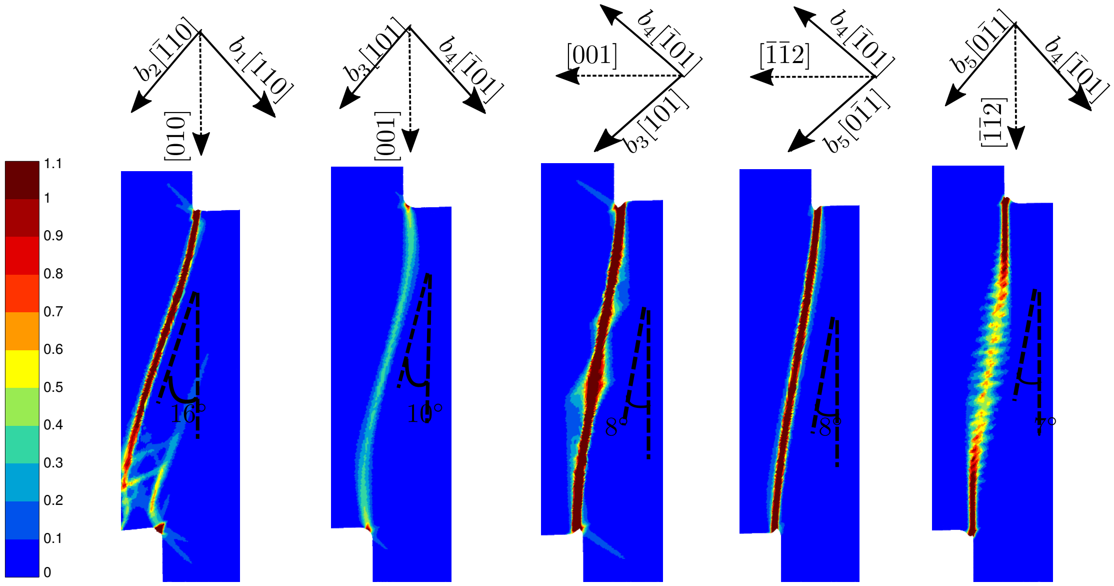

(a) (b) (c) (d) (e)

Fig. 10: Contour plots of cumulative plastic strain γ_{cum} in the shear region with *adiabatic* heating using the micromorphic crystal plasticity model (T_i = 923K, A = 0.004N) for (a) [100] − [010], (b) [110] − [001], (c) [001] − [110], (d) $[\bar{1}\bar{1}2]$ − [111], and (e) [111] − $[\bar{1}\bar{1}2]$ initially oriented crystals. The fields are shown at loading steps corresponding to the circles in Fig. 8. Compensation of the loading direction by Burgers vector of the activated slip systems is also shown.

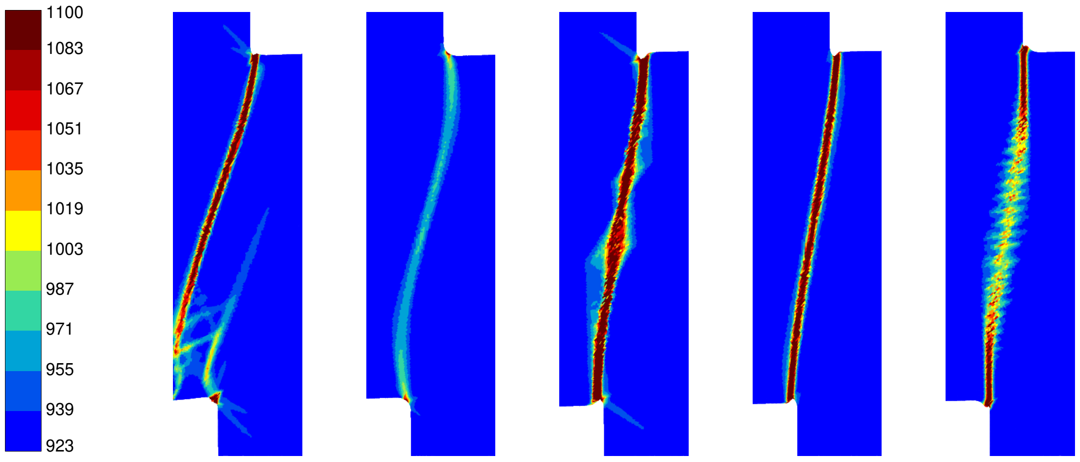

(a) (b) (c) (d) (e)

Fig. 11: Contour plots of temperature using the micromorphic crystal plasticity model (T_i = 923K, A = 0.004N) in the shear region for (a) [100] − [010], (b) [110] − [001], (c) [001] − [110], (d) [$\bar{1}\bar{1}2$] − [111], and (e) [111] − [$\bar{1}\bar{1}2$] initially oriented crystals. The fields are shown at the loading steps corresponding to the circles in Fig. 8.

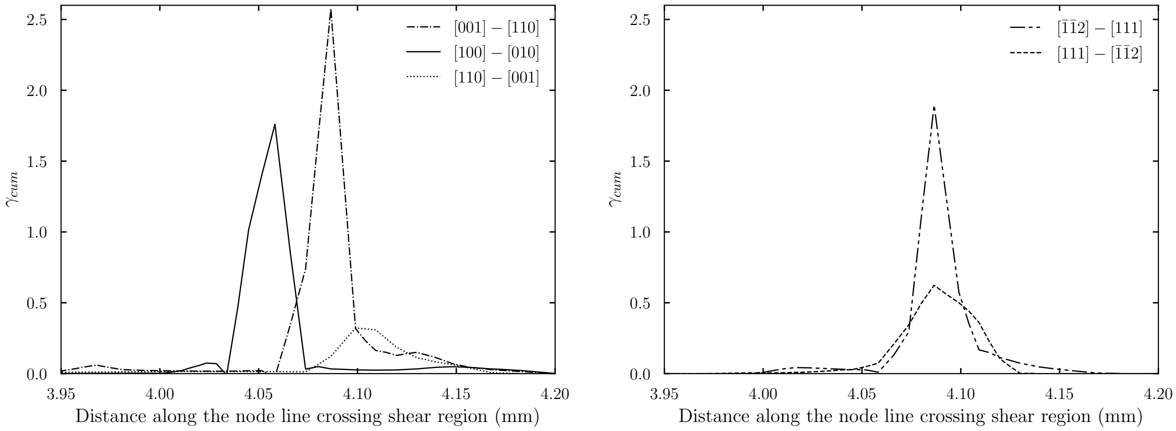

(a) (b)

Fig. 12: Cumulative plastic strain variation along the node line crossing the shear region (see Fig. 4) with *adiabatic* heating using the micromorphic crystal plasticity model (T_i = 923K, A = 0.004N) for (a) symmetric, and (b) asymmetric crystal orientations. The variation of cumulative plastic strain is plotted at loading steps corresponding to the circles in Fig. 8.

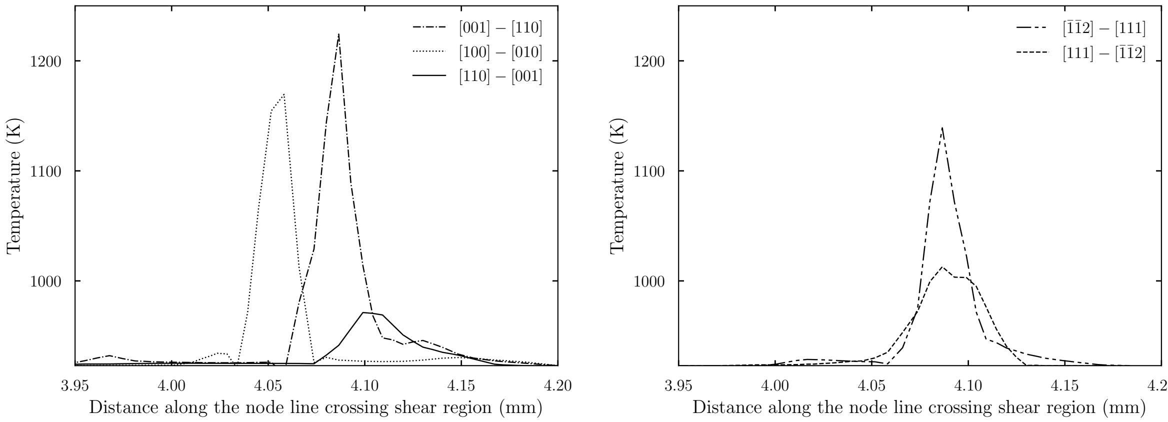

(a) (b)

Fig. 13: Temperature variation along the node line crossing the shear region for (a) symmetric, and (b) asymmetric crystal orientations. The variation of temperature across the shear band is plotted at loading steps corresponding to the circles in Fig. 8.

using the polar decomposition of the elastic part of the deformation gradient $\underset{\sim}{\boldsymbol{F}}^e$ into elastic rotation tensor $\underset{\sim}{\boldsymbol{R}}^e$ and the elastic right stretch tensor $\underset{\sim}{\boldsymbol{U}}^e$ as $\underset{\sim}{\boldsymbol{F}}^e = \underset{\sim}{\boldsymbol{R}}^e \cdot \underset{\sim}{\boldsymbol{U}}^e$. For small elastic distortions usual in metals, the elastic rotation tensor $\underset{\sim}{\boldsymbol{R}}^e$ is interpreted as the lattice rotation. The corresponding lattice rotation angle ϕ is computed as

$$\phi = \arccos\left[\frac{1}{2}\left(\mathrm{tr}(\underset{\sim}{\boldsymbol{R}}^e) - \underset{\sim}{\boldsymbol{1}}\right)\right]. \tag{48}$$

The lattice rotation fields for the various initially oriented crystals are shown in Fig. 14. The rotation of crystal lattice in the fully formed shear band is different for each considered initially oriented crystal and increases with increase in deformation. The discontinuous lattice rotation field is observed in [001] − [110] and [111] − [$\bar{1}\bar{1}$2] initially oriented crystals as a consequence of the complex plastic strain fields observed in Fig. 10. In comparison, single lattice rotation bands with smaller magnitude are observed for the [100] − [010], [110] − [001] and [$\bar{1}\bar{1}$2] − [111] crystal orientations. Some lattice rotation field patterns are reminiscent of kink banding structures studied in (Marano et al., 2021) but the situation is more complicated in the shear bands due to the simultaneous activation of several slip systems.

4.5.4. Effect of the gradient parameter A on shear band structure

The cumulative plastic strain γ_{cum} fields and formed ASB for the three different values of the gradient parameter A are shown in Fig. 15. With a decreasing value of A, the severity of plastic strain localization within the shear band increases, and a significant thermal softening is observed in the post-localization regime (see Fig. 16a). The effect of parameter A on the width of the shear bands can be seen from Fig. 16b. As expected from the analytical expression of the characteristic length scale, Eq. (47), the width of the shear band decreases with decrease in A value. The observed widths of the shear band with three different values of A, 0.04N, 0.02N, and 0.004N are found to be 0.085

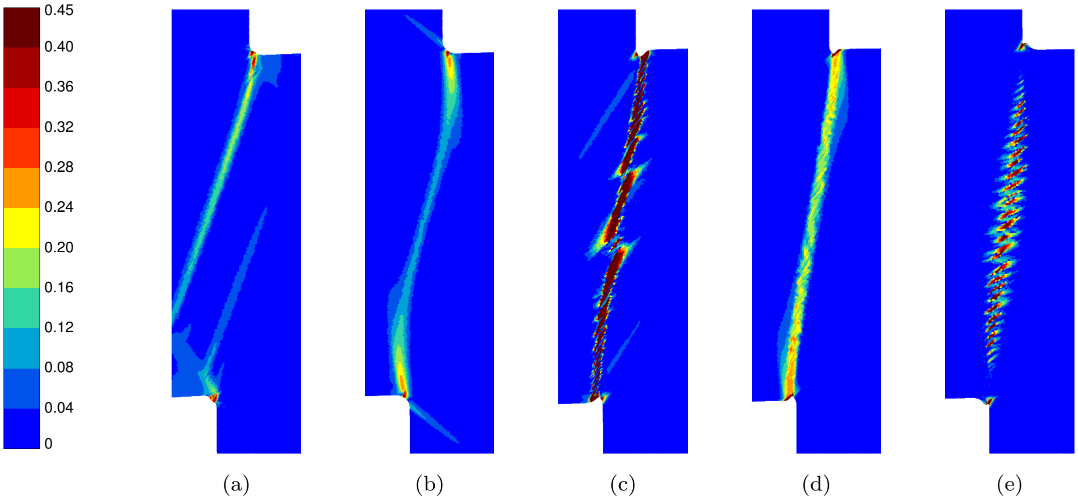

Fig. 14: Contour plots of lattice rotation fields in the shear region ($T_i = 923K$, $A = 0.004$N) for (a) $[100]-[010]$, (b) $[110]-[001]$, (c) $[001]-[110]$, (d) $[\bar{1}\bar{1}2]-[111]$, and (e) $[111]-[\bar{1}\bar{1}2]$ initially oriented crystals subjected to *adiabatic* heating. Fields are shown at loading steps corresponding to the circles in Fig. 8.

mm, 0.07 mm, and 0.05 mm, respectively.

5. Application to polycrystalline hat-shaped specimens

In this section, the micromorphic crystal plasticity model is applied to study the ASB formation in polycrystalline hat-shaped specimens. The single crystal constitutive behavior used in the numerical simulations is elastic-perfectly plastic and involves the same parameter values as in the previous sections. The material parameters used in the simulations are given in Table 3 and 4. First, orientation dependency of the shear band formation is investigated. Next, the grain size effect is predicted in the *isothermal* case. Then, the effect of *adiabatic* heating on the resulting load is evaluated for the considered polycrystalline aggregates. The temperature evolution due to *adiabatic* heating is computed using the expression in *case 2* presented in section 2.2 (Eq. (40)). Finally, the grain size effect on shear band width is predicted by the micromorphic model.

5.1. Polycrystal generation and finite element meshing

Polycrystalline aggregates generated by the Voronoi tessellation using the polycrystal generation package Neper (Quey and Renversade, 2018) are shown in Fig. 17 and 18. The application of Voronoi tessellation to create an actual geometry with the grains is a powerful tool to predict grain size effects, for example on the overall mechanical response of the material under deformation. Two polycrystalline aggregates, namely the *coarse-grained* and *fine-grained* with an average grain size of 0.80 mm and 0.15 mm, respectively, are generated. The smallest grain size in the shear region of the generated polycrystalline aggregates is 0.38 mm and 0.10 mm, respectively. Moreover, the pole

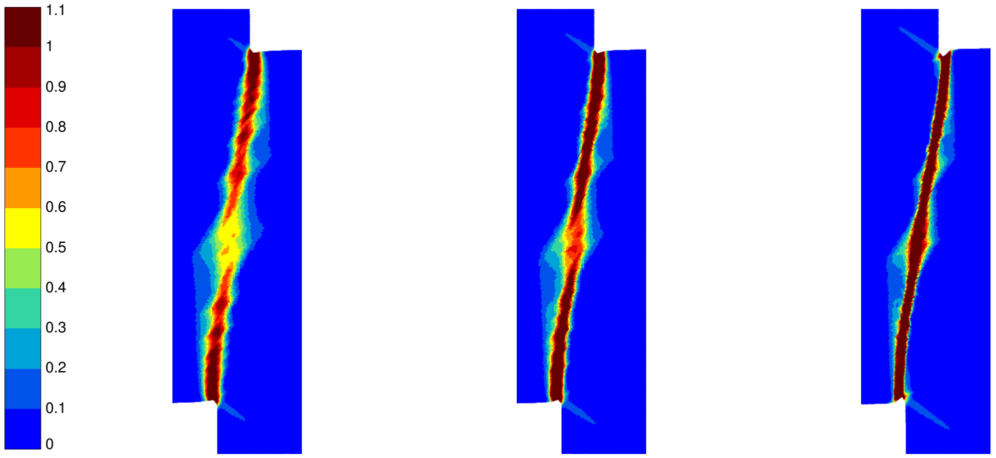

(a) (b) (c)

Fig. 15: Contour plots of cumulative plastic strain γ_{cum} using the micromorphic crystal plasticity model ($T_i = 923$K) with three different values of (a) $A = 0.04$N, (b) $A = 0.02$N, and (c) $A = 0.004$N. Fields are shown for the $[001] - [110]$ initially oriented crystal subjected to *adiabatic* heating. Fields are shown at a normalized displacement of 0.06 mm/mm

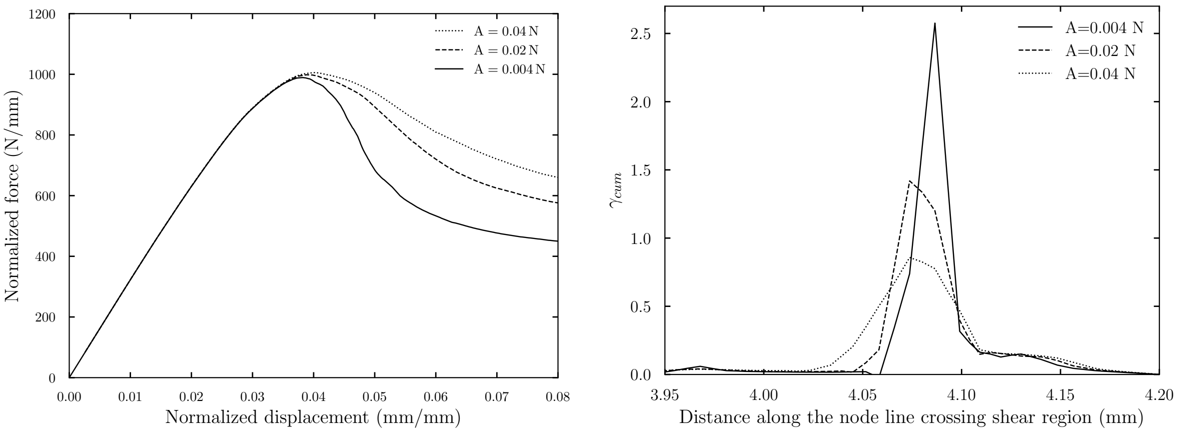

(a) (b)

Fig. 16: Effect of different values of the gradient parameter A on the (a) load-displacement curves, and (b) cumulative plastic strain γ_{cum} variation along the node line crossing the shear region for $[001] - [110]$ initially oriented crystal plotted at a normalized displacement of 0.06 mm/mm.

figure showing the crystallographic texture for each realization is plotted by means of the open-source software toolbox MTEX (Bachmann et al., 2010).

Mesh independent numerical results are ensured using fine enough mesh size within the grains of the shear region combined with the use of the micromorphic crystal plasticity model. Meshing is performed using an open-source package Gmsh (Geuzaine and Remacle, 2009). A bottom-up approach is used for the meshing, i.e., in the order of 0D, 1D, and 2D entities (i.e., vertices, edges, and polygons) for the 2D simulations under plane strain conditions (Quey et al., 2011).

The applied boundary conditions in the present polycrystalline simulations were described in section 4.3. In addition, each realization of polycrystalline aggregate is assigned with different random crystal orientations. No special interface condition is applied to grain boundaries. The interface conditions arise from balance equations in the continuum model: Continuity of the displacement vector components, and continuity of the traction vector components at least in the weak form according to the finite element method.

In the present work, the microslip γ_χ is assumed to be continuous at the interface. The surface traction ($\underline{\boldsymbol{T}}$) and generalized surface traction (M) in Eq. (21) are also continuous. There are alternative interface conditions like the *microhard* conditions assuming vanishing microslip at the boundaries, and *microfree* interface conditions enforcing vanishing generalized (higher order) tractions at the grain boundaries. The former and latter grain boundary conditions respectively provide upper and lower values of the overall response of the polycrystal (Gurtin and Needleman, 2005; Bargmann et al., 2010). However, these two interface conditions are not applicable to all sorts of interface behavior. One approach to obtain interface behavior inbetween these two extreme conditions is by introducing *interface energy* as in (Aifantis and Willis, 2005). The continuity requirements chosen in the present work also provide intermediate values for the polycrystal response. More general interface conditions have been proposed allowing for the transition from microhard conditions to microfree (or constant generalized tractions) once a threshold is reached at the grain boundary (Wulfinghoff et al., 2013). In the case of a plastically deforming grain and an elastic neighboring grain, the micromorphic model leads to a smooth transition of the microslip variable γ_χ to zero in a boundary layer in the elastic phase. This means that the amounts of slip are zero in the elastic grain but it is not necessarily the case for the micromorphic variable. This situation is more complicated to describe in a strict strain gradient crystal plasticity model. In contrast, in the micromorphic approach, the slip variables are discontinuous whereas the microslip is continuous. This situation was discussed in (Cordero et al., 2010).

5.2. Results and discussion

5.2.1. Grain orientation dependency of the shear band

The effect of grain orientations on the shear band predicted by the numerical simulations is investigated first for polycrystalline aggregates subjected to *isothermal* deformation using the micromorphic crystal plasticity model. Two distinct crystal orientation distributions are assigned to the grains in

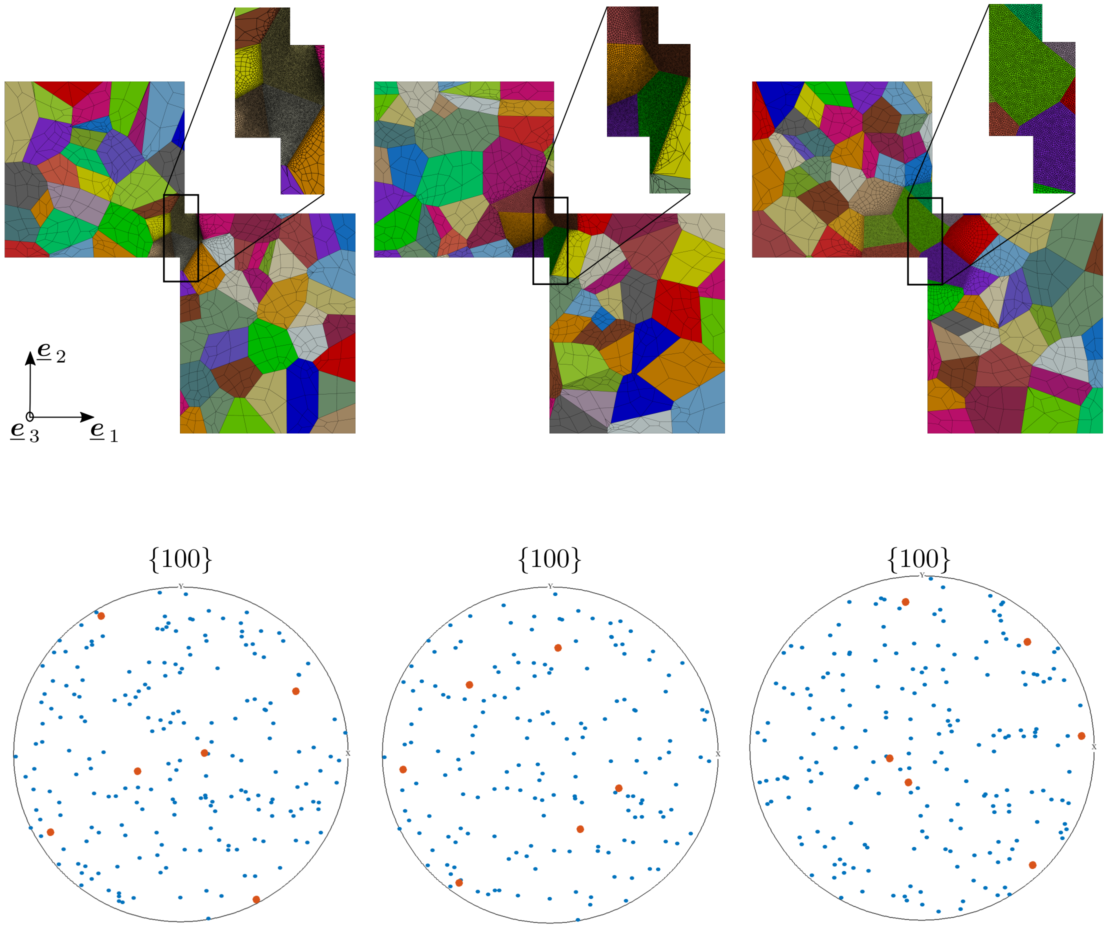

(a)

(b)

(c)

Fig. 17: Different realizations of the *coarse-grained* polycrystalline aggregates and corresponding pole figures: (a) Realization 1, (b) realization 2, and (3) realization 3. Colors represent individual grains and the red points in pole figures denote the orientation assigned to the grains in the shear region.

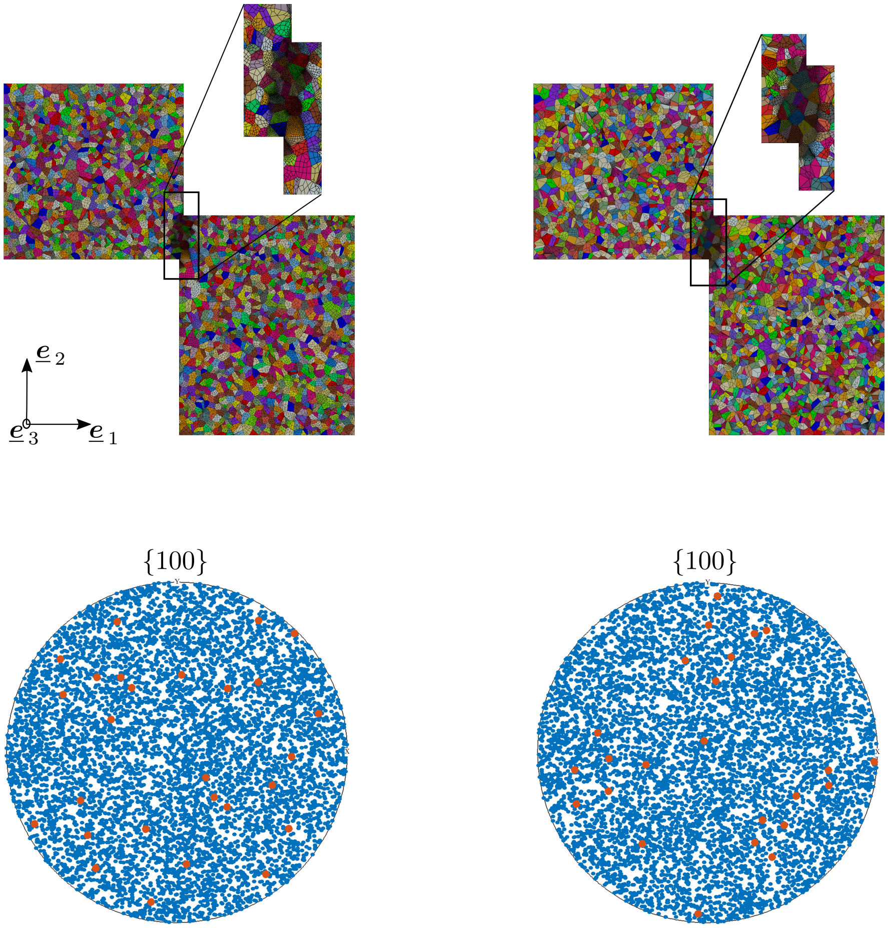

(a)

(b)

Fig. 18: Different realizations of the *fine-grained* polycrystalline aggregates and corresponding pole figures: (a) Realization 1, and (b) realization 2. Colors represent individual grains and the red points in the pole figures denote the orientation assigned to the grains in the shear region.

the shear region, namely the *orientation 1* and *orientation 2*. The realizations of the *coarse-grained* and *fine-grained* polycrystalline aggregates with corresponding pole figures are shown in Fig. 19a and 19b, respectively. The predicted load-displacement curves for the *coarse-grained* and *fine-grained* polycrystalline aggregates are given in Fig. 20a and 20b, respectively. As shown in these figures, the resulting load required to deform the *orientation 2* in both polycrystalline aggregates is greater than the *orientation 1*, which indicates that the development and propagation of the shear band highly depends on the orientation of the grains crossed by the bands, grain boundaries acting as obstacles to shear band propagation. In *orientation 1* case, the orientations of the grains in the shear region are such that they favor plastic flow and subsequent shear band formation compared to *orientation 2*. Furthermore, less orientation dependency is observed in the *fine-grained* polycrystalline aggregates compared to the *coarse-grained* polycrystalline aggregates (see Fig. 20b). The formed shear bands are shown in Fig. 21. More significant strain localization is observed in *orientation 1* than in *orientation 2*. This indicates that some grains in *orientation 1* represent stronger obstacles to shear band transmission from grain to grain. This effect is reduced when a larger number of grains are available along the shear band path.

5.2.2. Grain size effect in the polycrystalline hat-shaped specimens

There are mainly two types of size effects to be considered, which are responsible for the increased strength of polycrystalline aggregates compared to single crystals, namely the ‘specimen size’ effect and ‘grain size’ effect (Armstrong, 1961). The specimen size effect occurs when there are few grains in the specimen cross-section. It is mainly related to the orientation dependency of the crystal plastic flow, as demonstrated in the previous subsection about the influence of number of grains along the shear band path. On the other hand, the ‘grain size’ effect occurs when there are sufficiently many grains in the specimen cross-section. In addition to the orientation dependence of the plastic flow within the grains, internal stress concentration takes place at the grain boundaries and causes yielding and subsequent plastic flow (Armstrong, 1961). The well-known grain size effect in a polycrystalline material is the Hall-Petch size effect, which indicates that the yield strength of material is inversely proportional to the square root of grain size (Hall, 1951; Petch, 1953). Numerically, strain gradient plasticity models can be used to predict the grain size effects in polycrystalline materials, as done for instance in (Acharya and Beaudoin, 2000; Evers et al., 2004; Aifantis and Willis, 2005; Borg, 2007).

In the present work, firstly, the grain size effect is studied in the *isothermal* case for polycrystalline hat-shaped specimens. The realizations of polycrystalline aggregates investigated are shown in Fig. 17b and 18a for the *coarse-grained* and *fine-grained* polycrystalline aggregates, respectively. The shape and geometry of the hat-shaped specimen are such that it allows for the spontaneous formation of a shear band even in the absence of thermal softening in the numerical simulations due to the perfectly plastic crystal behavior. The cumulative plastic strain fields with the classical and micromorphic crystal plasticity models are shown in Fig. 22. The classical crystal plasticity model, which does not feature any characteristic length scale, exhibits a pathological mesh dependency and the width

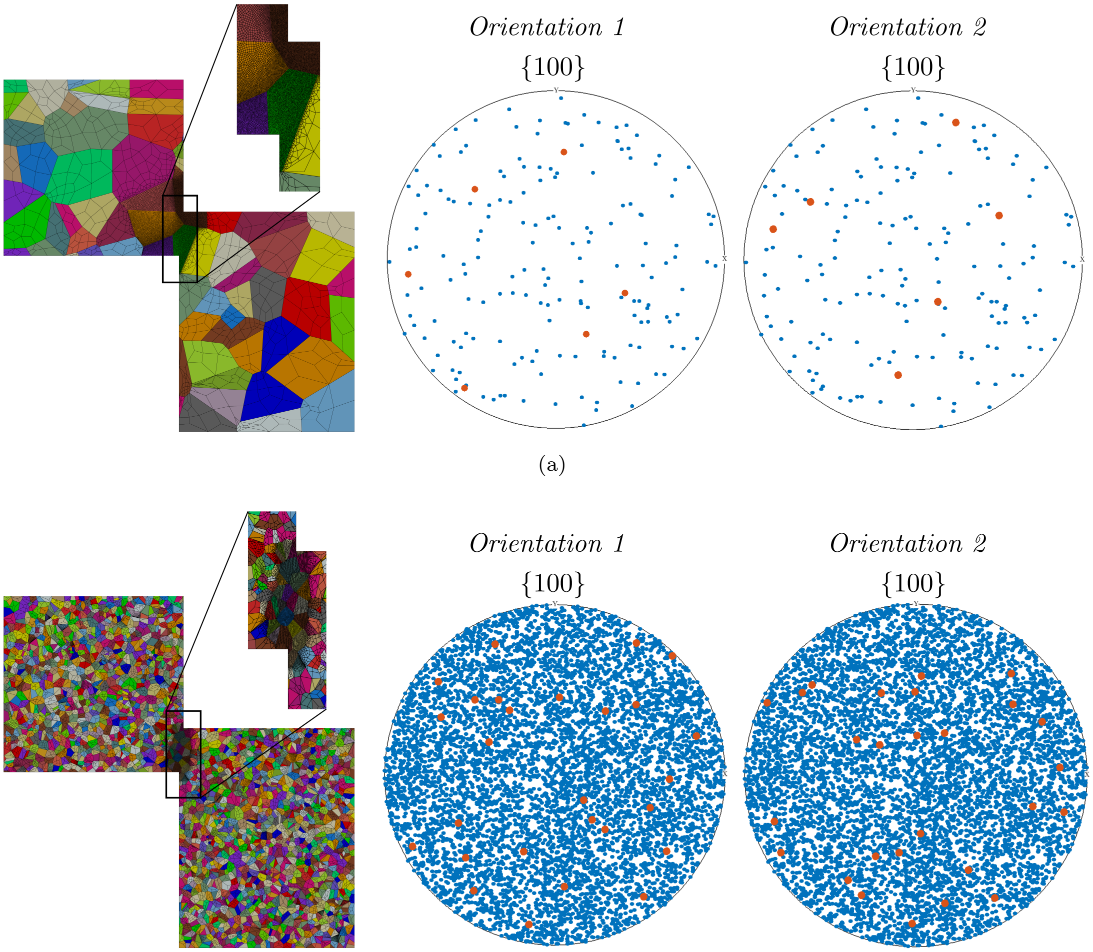

(a)

(b)

Fig. 19: Polycrystalline aggregates with two distinct orientation distributions assigned to the grains in the shear region (*orientation 1* and *orientation 2*) for the (a) *coarse-grained*, and (b) *fine-grained* with corresponding pole figures. The red points in the pole figure denote the orientations assigned to the grains in the shear region

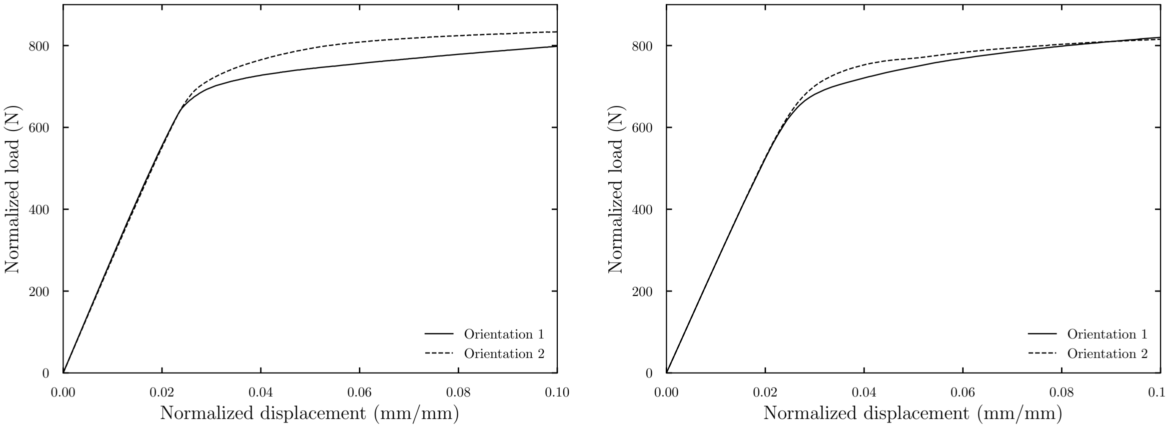

(a) (b)

Fig. 20: Effect of the change in orientation of the grains in the shear region on the load-displacement curve using the micromorphic crystal plasticity model ($A = 0.04$N) for the (a) *coarse-grained* polycrystal aggregate, and (b) *fine-grained* polycrystal aggregates subjected to *isothermal* conditions.

of the formed shear band collapses to one element size (more precisely one Gauss point size, see Fig. 22a and 22b). Therefore, the classical crystal plasticity models cannot be used to study strain localization problems in polycrystals. In contrast, the width of the formed shear band predicted by the micromorphic crystal plasticity model is finite, see Fig. 22c and 22d. The normalized load-normalized displacement curves using the classical and micromorphic crystal plasticity models in the isothermal case are shown in Fig. 23. The predicted size effect is linked to the characteristic length scale ℓ_c through the gradient parameters A and H_χ as in Eq. (47). The micromorphic crystal plasticity model merely influences the hardening rate and does not affect the initial yield strength. This is because any gradient plasticity formulation based on a quadratic potential with respect to the gradient of plastic distortion cannot result in an increase in yield strength but only increases the hardening rate. The initial yield can be influenced by rank one potentials according to (Wulfinghoff et al., 2015) or using the recent approach by (Steinmann et al., 2019). The grain size effect is associated with spatial strain gradients inside the grains because of the heterogeneous plastic deformation resulting from grain-to-grain plastic strain incompatibilities. The grain boundaries act as obstacles to dislocation motion, and the strain gradient-induced GNDs pile up at grain boundaries. In addition, with the decrease in grain size, the area at the grain boundaries with GNDs density increases and leads to increased local stresses and of the resulting load. The larger number of grain boundaries in the shear region of the *fine-grained* polycrystalline aggregates obstructs the initiation and subsequent plastic flow and results in a higher resulting load.

Moreover, the effect of grain size on the load-carrying capacity subjected to *adiabatic* heating condition is now studied. Simulations are performed with two different values of the gradient parameter A, namely 0.004N, and 0.04N. The corresponding load-displacement curves for the realizations of the *coarse-grained* and *fine-grained* polycrystalline aggregates are given in Fig. 24a, 24b and Fig. 24c

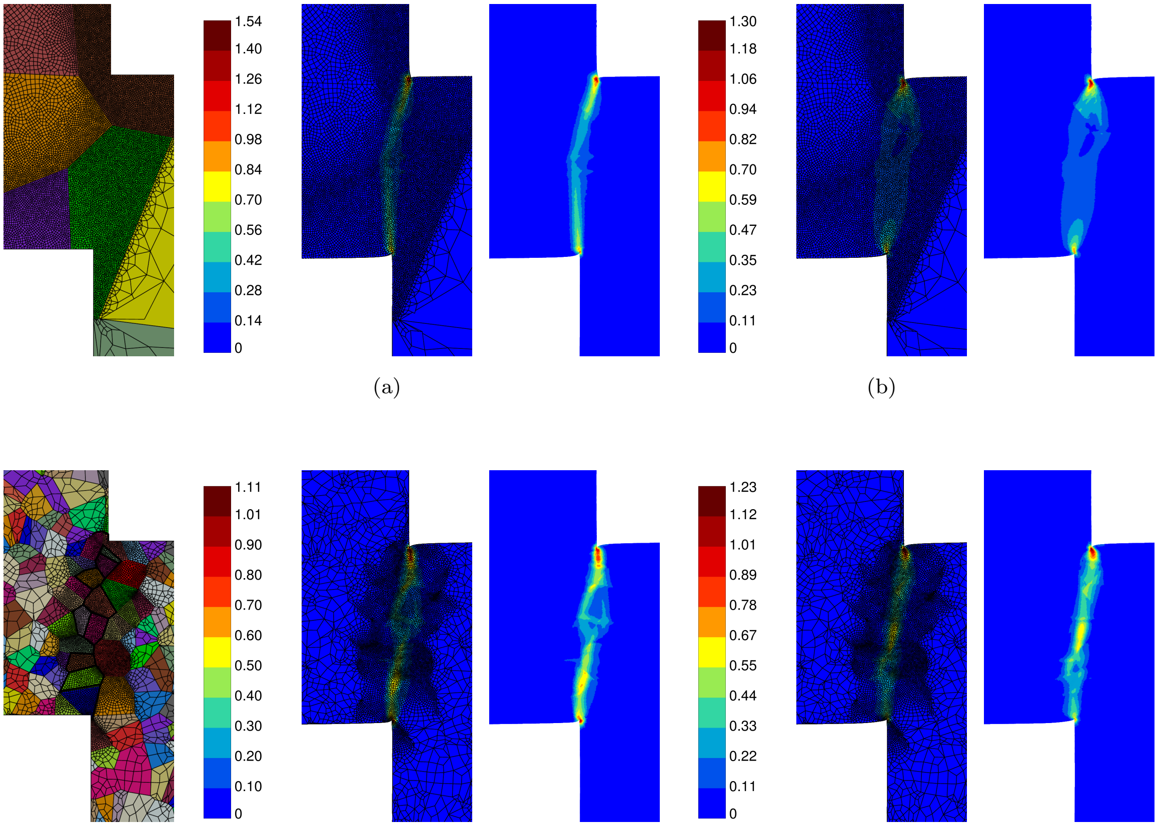

(a) (b)

(c) (d)

Fig. 21: Contour plots of cumulative plastic strain γ_{cum} using the micromorphic crystal plasticity model ($A = 0.04$N) for the (a) *coarse-grained* polycrystalline aggregates assigned with *orientation 1*, and (b) *orientation 2*. (c) The *fine-grained* polycrystalline aggregates assigned with *orientation 1*, and (d) *orientation 2*. Fields are shown at the normalized imposed displacement of 0.06 mm/mm under *isothermal* conditions (T_i=923K). For clarity the fields are shown with and without the finite element mesh.

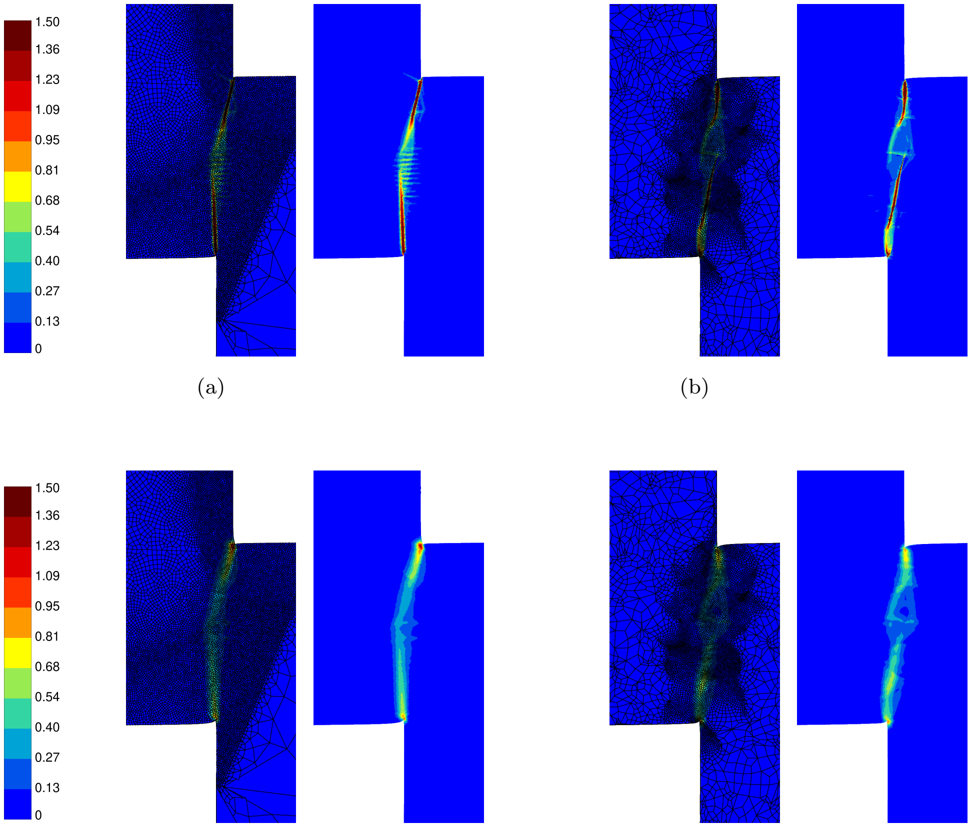

(a) (b)

(c) (d)

Fig. 22: Contour plots of cumulative plastic strain γ_{cum} using (a) the classical crystal plasticity model in *coarse-grained (orientation 1)*, and (b) *fine-grained (orientation 1)* polycrystalline aggregates, (c) using the micromorphic crystal plasticity model (A=0.04 N) in *coarse-grained (orientation 1)*, and (d) *fine-grained (orientation 1)* polycrystalline aggregates. Fields are shown at a normalized displacement of 0.06 mm/mm and under *isothermal* conditions.

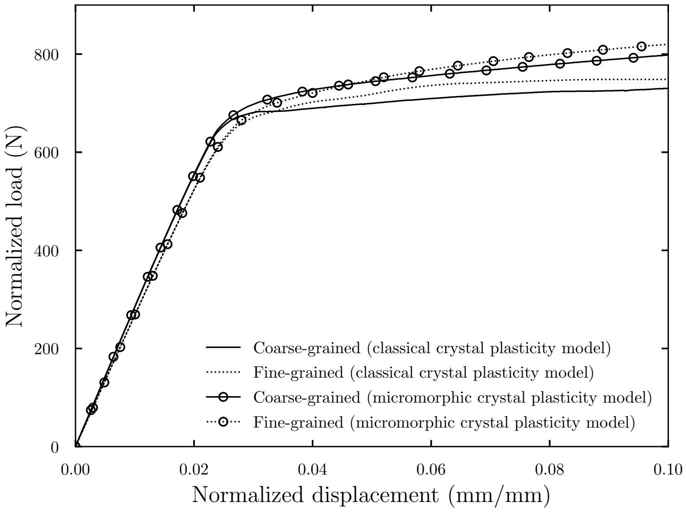

Fig. 23: Load-displacement curves obtained using the classical and micromorphic crystal plasticity models for the *coarse-grained* (realization 2), and *fine-grained* (realization 1) polycrystalline aggregates (hat–shaped specimens under isothermal conditions).

and 24d, respectively. The load-displacement curves exhibited by the different realizations of each polycrystalline aggregate with the same gradient parameter A are distinct from each other because of the assigned different random orientations and distinct shape of the grains in the shear region. A broader dispersion of the resulting loads is observed in realizations of the *coarse-grained* polycrystal aggregates (see Fig. 24a and 24b) compared to *fine-grained* polycrystal aggregates (see Fig. 24c and 24d). It is found that the average resulting load in *fine-grained* polycrystal aggregate remain below the *coarse-grained* polycrystal aggregate as seen from the average curves in Fig. 24e and 24f. This is probably due to the insufficient number of realizations which does not allow for statistical representativity. The results also show that higher values of A parameters lead to a reduced softening of the overall curves.

5.2.3. Effect of grain size on the shear band width

In this section the grain size effect on the width of shear bands is studied under *adiabatic* heating conditions. In the present polycrystalline simulations, deformation is highly localized within the grains of the shear region. Moreover, the grain size in the shear region plays a crucial role in the shear band formation. The shear band is triggered at the corners of the specimen, and strongly heterogeneous plastic deformation takes place between the corners. Furthermore, it is observed that some grains exhibit a larger amount of shear, while other grains remain almost undeformed. The formation of the shear band in *coarse-grained* polycrystalline aggregates for the realizations 1 and 3 (Fig. 25a and 25c) is restricted probably due to the unfavorable orientations of the grains in the shear region. In contrast, the shear band is easily formed in the realization 2 as seen from Fig. 25b. The orientation dependency in the shear band formation is the main reason for the wide dispersion of the resulting loads observed in *coarse-grained* polycrystalline aggregates. In contrast, in *fine-grained* polycrystalline aggregates, plastic flow in some grains is limited because of their grain boundaries and the orientation of the neighboring grains, causing subsequent plastic flow in more favorable grains as seen from Fig. 26a. However, less orientation dependency of the grains in the shear region is observed in the *fine-grained* polycrystalline aggregates compared to *coarse-grained* (see Fig. 26a and 26b). Fig. 27a and 27b show the cumulative plastic strain γ_{cum} variation along a node line crossing the shear region for the *coarse-grained* polycrystalline aggregates using gradient parameters $A = 0.004$ N and $A = 0.04$ N, respectively. Significant strain localization is observed for lower values of A, i.e., 0.004N compared to 0.04N. Fig. 27c and 27d show the cumulative plastic strain variation along the node line crossing the shear region for *fine-grained* polycrystalline aggregates with $A = 0.004$N and $A = 0.04$N, respectively. The shear band width is defined by the following criterion: The region in which the cumulative plastic strain is larger than 10% of the peak value. The measured widths of the shear band for the *coarse-grained* and *fine-grained* polycrystalline aggregates with the gradient parameter A of 0.004N, and 0.04N are given in Table 8. A larger dispersion of the shear band width is observed in the *coarse-grained* polycrystal realizations compared to the *fine-grained*, in a way similar to the predicted resulting loads.

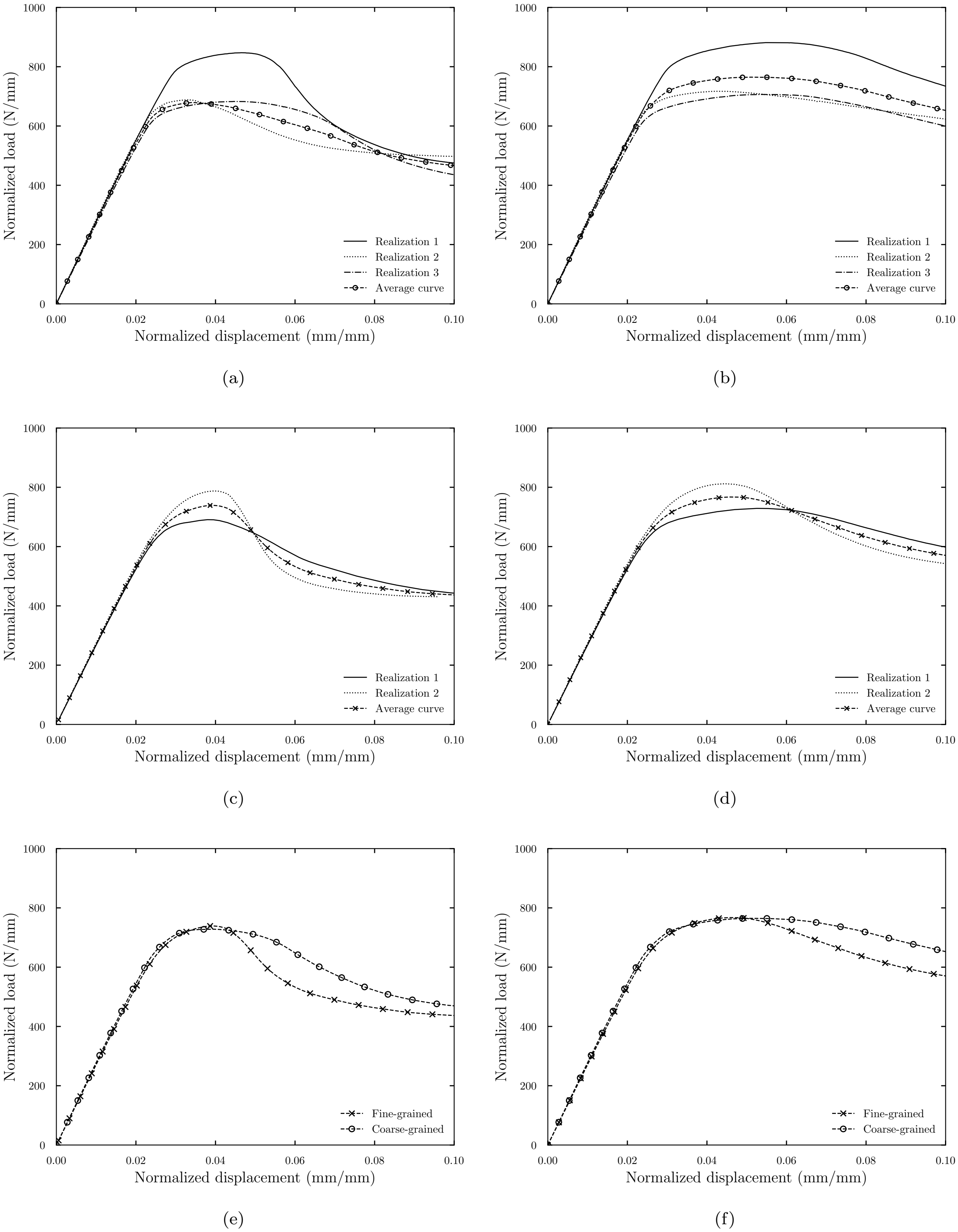

(a)

(b)

(c)

(d)

(e)

(f)

Fig. 24: Load-displacement curves using the micromorphic crystal plasticity model for various realizations of the polycrystalline aggregates subjected to *adiabatic* heating conditions: (a) the *coarse-grained* polycrystalline aggregates with $A = 0.004\text{N}$, and (b) $A = 0.04\text{N}$, (c) the *fine-grained* polycrystalline aggregates with $A = 0.004\text{N}$, and (d) $A = 0.04\text{N}$, (e) Average load-displacement curves with $A = 0.004\text{N}$, and (f) $A = 0.004\text{N}$.

The measurement of the shear band width along one single node line may not be sufficient in polycrystalline simulations. Therefore, the surface of the elements satisfying a specific criterion is calculated using the post-processing technique. The surface of the elements having cumulative plastic strain more than 10% of the peak value is measured. Finally, the width of the shear band w is calculated by dividing the surface of the band by the shear zone height h (see section 4.3 for specimen dimensions). The obtained values of the shear band widths are given in Table 8. The two definitions of shear band with provide similar results. Typical values of 50 micron (resp. 100 micron) are found for $A = 0.004$ N (resp. $A = 0.04$ N) irrespective of the grain size.

The present simulations are limited to adiabatic conditions although it is well–known that heat conduction can also contribute to the band structure (Lemonds and Needleman, 1986; Medyanik et al., 2007; Mcauliffe and Waisman, 2013; Wcisło and Pamin, 2017a,b). It is worth checking the typical lengths associated with heat conduction under the strain rate conditions of the simulations. The characteristic length of heat diffusion during a time interval t can be estimated as $\sqrt{kt/\rho C_p}$. The parameter values considered in the work and time interval of one second result in diffusion distances of the order of 1 mm. This shows that heat conduction induced length scale is in competition with the microstructure related one. Adiabatic conditions are therefore a strong assumption in the present simulations. This pleads for coupling the present model to heat conditions in future work. This also strongly depends on the strain rate and grain size ranges in the simulations. The diffusion term in heat equation has a regularizing effect even though the involved length scales are sometimes too small for efficient FE modeling, as discussed in (Wcisło and Pamin, 2017a). However, the strain gradient plasticity model should not be solely seen as a regularization method. It also introduces in the modeling microstructure aspects related to dislocation activity like pile-up formation and ensuing grain size effects, as studied in the present work. As mentioned in the introduction, Zhu et al. (1995); Tsagrakis and Aifantis (2015) analytically derived two characteristic lengths emerging from the coupling of strain gradient plasticity. The first one is related to the ratio of the strain gradient plasticity parameter and the hardening modulus. The second one involves the heat conductivity and strain gradient plasticity parameters. We have evaluated these length scales for the parameter values used in the present work. The second length scale is found to be close to 100 micron which confirms the importance of heat conduction and the competition with the microstructural length.

6. Conclusions

The numerical simulation work presented here was intended to provide an insight into the mechanism of strain localization in single and polycrystalline FCC metallic materials under adiabatic conditions. The main findings obtained in this contribution can be summarized as follows:

1. A thermodynamically consistent constitutive framework for the micromorphic crystal plasticity model was used to derive temperature evolution under adiabatic conditions.
2. The micromorphic crystal plasticity model pursues the objective of regularization of the adiabatic shear band formation.

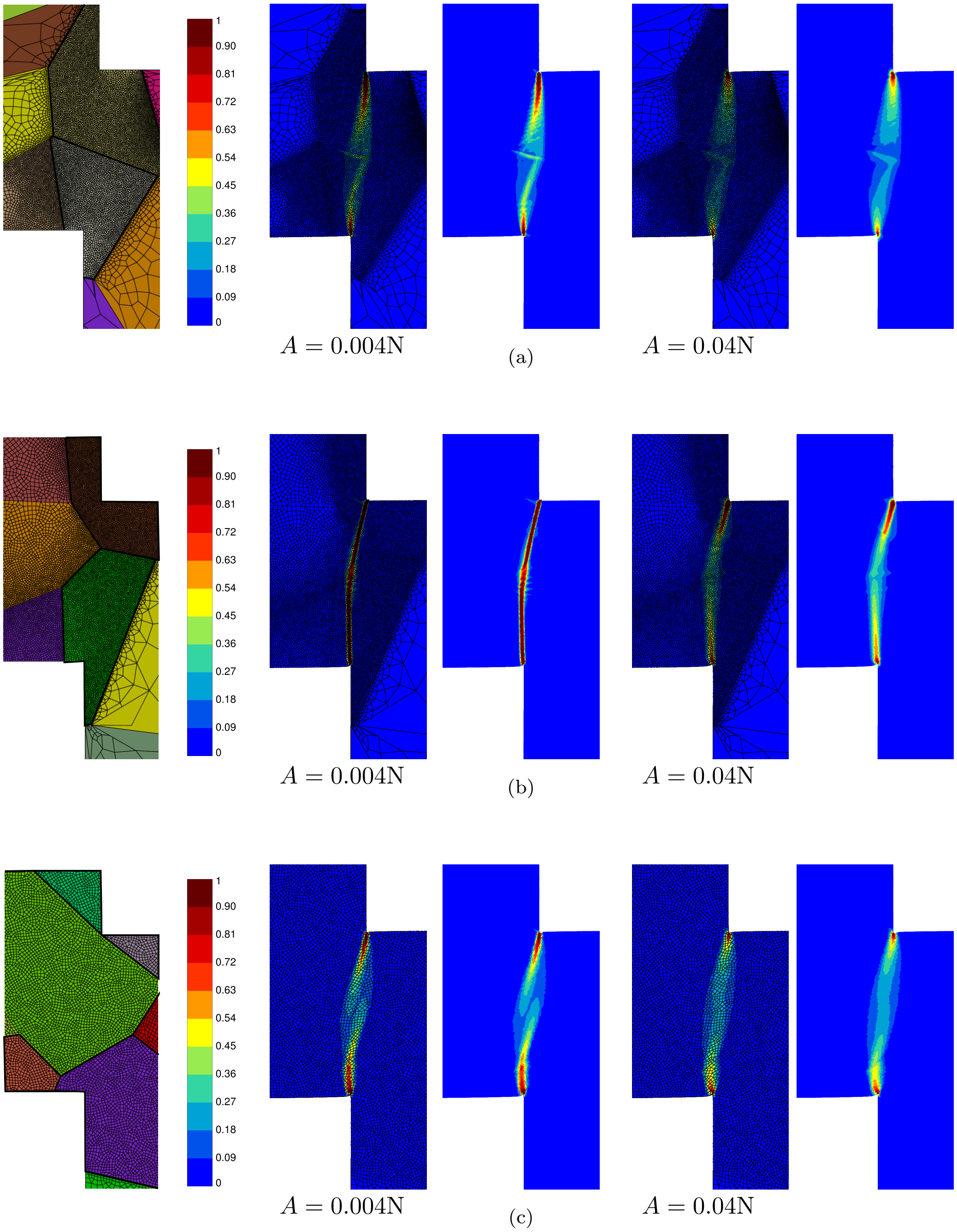

Fig. 25: Contour plots of cumulative plastic strain γ_{cum} in the *coarse-grained* polycrystalline aggregates subjected to *adiabatic* heating using the micromorphic crystal plasticity model ($A = 0.004\text{N}$ and $A = 0.04\text{N}$) for three different realizations (a) realization 1, (b) realization 2, and (c) realization 3. Fields are shown at a normalized displacement of 0.052 mm/mm.

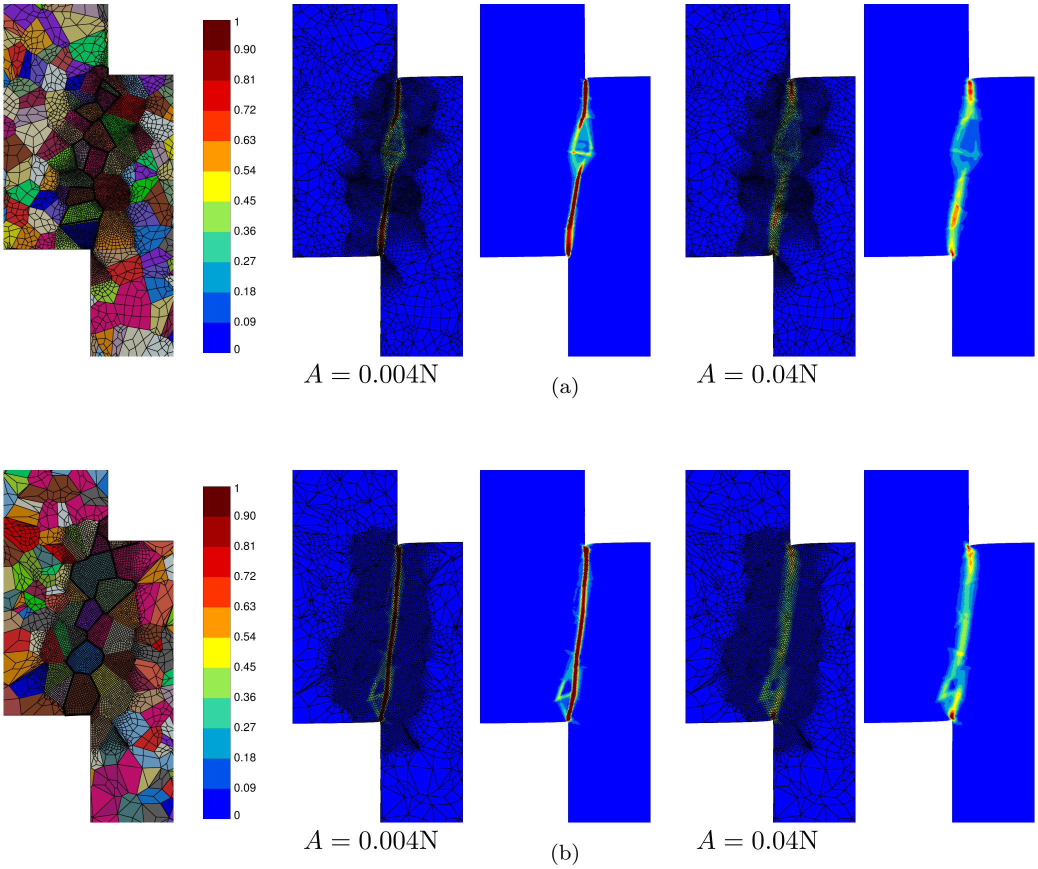

(a)

(b)

Fig. 26: Contour plots of cumulative plastic strain γ_{cum} in the *fine-grained* polycrystalline aggregates subjected to *adiabatic* heating using the micromorphic crystal plasticity model ($A = 0.004$N and $A = 0.04$N) for two different realizations (a) realization 1, and (b) realization 2. Fields are shown at a normalized displacement of 0.052 mm/mm.

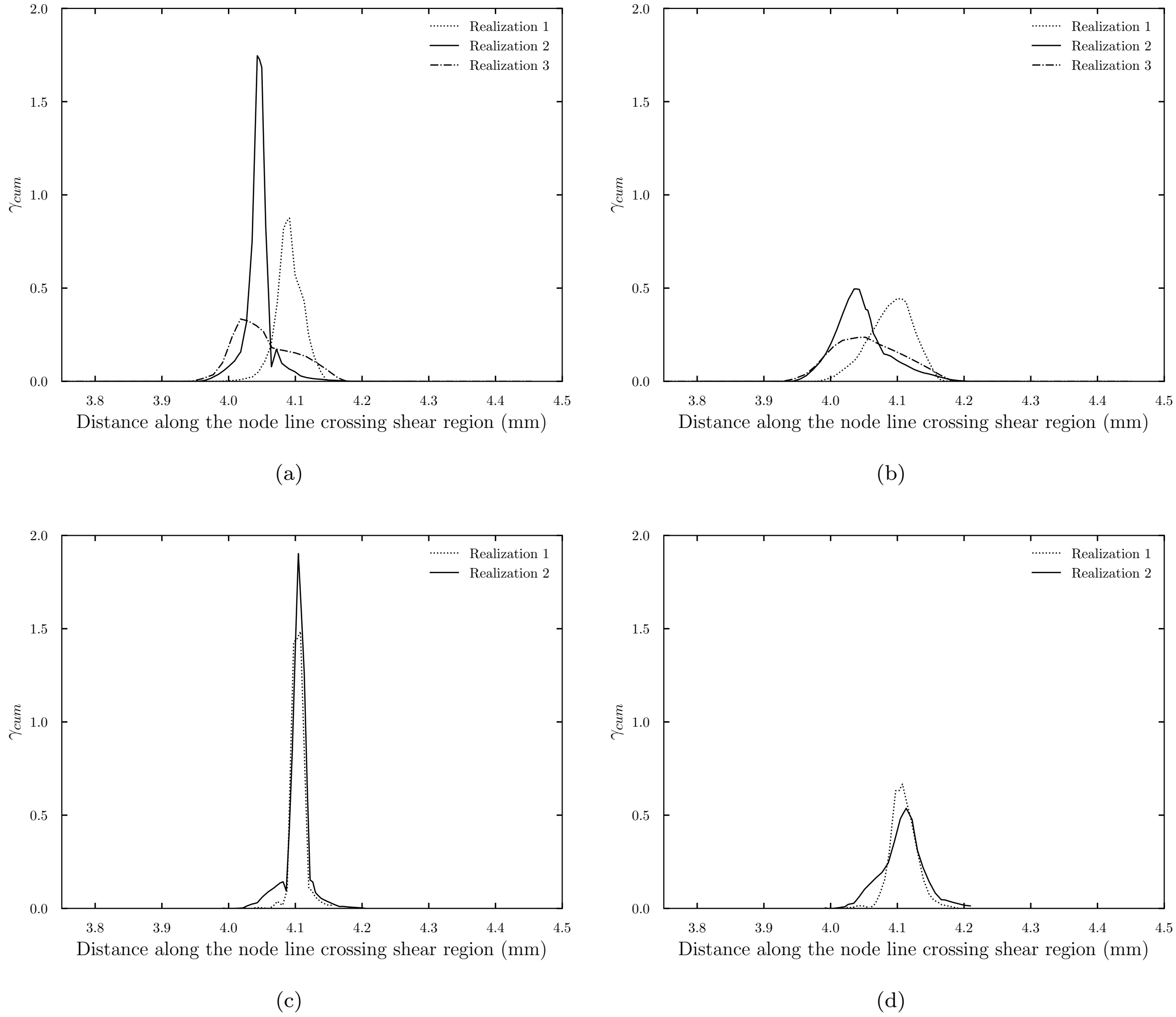

(a)

(b)

(c)

(d)

Fig. 27: Cumulative plastic strain variation along the node line crossing shear region using the micromorphic crystal plasticity model subjected to *adiabatic* heating in (a) *coarse-grained* polycrystalline aggregates with $A = 0.004$N, and (b) $A = 0.04$N. (c) The *fine-grained* polycrystalline aggregates with $A = 0.004$N, and (d) $A = 0.04$N. All the variations are plotted for the normalized displacement of 0.052 mm/mm.

Table 8: Shear band width w measured along the node line crossing the shear region and using a post-processing method.

coarse-grained	w (mm) ($A = 0.004$N)	w (mm) Post-processing ($A = 0.004$N)	w (mm) ($A = 0.04$N)	w (mm) Post-processing ($A = 0.04$N)
Realization 1	0.05	0.042	0.12	0.12
Realization 2	0.03	0.049	0.13	0.072
Realization 3	0.12	0.065	0.15	0.11
fine-grained				
Realization 1	0.03	0.036	0.05	0.12
Realization 2	0.03	0.033	0.05	0.098

3. The orientation of the formed ASB with respect to the loading axis is affected by the crystal initial orientation. $[100]-[010]$ crystal orientation shows the stiffest response to ASB formation. On the other hand, crystals initially oriented at $[111]-[\bar{1}\bar{1}2]$ show the lowest tendency to shear band formation, and no evident shear banding is observed. Moreover, it is observed that the formed shear band width depends on the initial crystal orientation.
4. The grain size effect, *namely the finer the grain size the higher the stress*, was illustrated in the response of polycrystalline FCC metallic materials using the micromorphic crystal plasticity model subjected to *isothermal* deformation. It is shown that the micromorphic crystal plasticity model merely influences the hardening rate but does not affect the initial yield strength.
5. The resulting load and the formation of shear band is highly orientation dependent in polycrystalline simulations in the case of *coarse grained* polycrystal. The favorable orientation of the grains in the shear region results in decreased resulting load and ease of shear band formation. Furthermore, wide dispersion of the resultant load and width of the shear band is observed in different realizations of the *coarse grained* polycrystalline aggregates.
6. The relation between observed shear band widths, intrinsic length scale of the micromorphic model and grain size was analyzed. It shows that the intrinsic length scale mainly controls the shear band width and that grain boundaries serve as obstacles to ASB propagation thus controlling the intensity of strain localization.

The purpose of the present work was not the analysis of the full ASB formation process which includes multiscale shear banding, heat conduction and dynamic effects. The objective is the analysis of anisotropic effects induced by crystal plasticity on strain localization phenomena under adiabatic conditions. It contains effects relevant to ASB formation but surely not all of them. Significant physical aspects of strain localization in crystalline solids under adiabatic conditions were highlighted, namely the anisotropic character of crystal plasticity, the associated microstructure effects and their consequence on shear band path and width. These specific aspects have not been studied in the previous literature and can give ideas for the design of shear banding resistant crystallographic textures by appropriate grain boundary engineering. Especially the shear band path and width were carefully described in single and polycrystals with proper account of hardening induced by GNDs and grain boundary and grain size effects. It is possible to predict stronger grain size effects in the polycrystalline simulations by considering larger number of grains in the shear region of the hat-shaped specimen. However, due to high computational costs, only two grain sizes were considered in the present work. Moreover, work-hardening was not included in the simulations to clearly isolate the micromorphic and grain size effects from classical hardening. The consideration of dislocation–based hardening in the future will require the evaluation of stored energy in order to evaluate temperature evolution under adiabatic conditions. It is common practice to consider a constant value 0.9 of the Taylor-Quinney parameter. However, the experimental evidence, for instance, (Kapoor and Nemat-Nasser, 1998; Rittel et al., 2012), showed that, in reality, its value can be much less than 0.9. The thermodynamically consistent framework of the constitutive equations for the gradient crystal plasticity (reduced-order micromorphic) model presented in this work must be extended to allow for evolving Taylor-Quinney parameters predicted by suitable free energy density functions. It is hoped that the predictions made in the present work will serve as incentives to perform experimental tests on single and oligo-crystalline hat–shaped specimens to precisely determine the relation between ASB width and grain size. The analysis of such tests may require the extension of the present computational approach to more realistic 3D computations.

Heat conduction was neglected in the present work although it plays a significant role at the grain scale for the strain rates and grain sizes considered in this work. Extension of the work considering the coupling of gradient crystal plasticity and heat conduction is therefore necessary in the future to highlight the competition between lengths emerging from microstructure and thermal effects. In addition, grain boundary sliding and decohesion are additional important deformation and damage mechanisms at high temperatures. They are not included in the present work but this is possible as demonstrated in (Musienko et al., 2004). Coupling strain gradient crystal plasticity and grain boundary sliding/opening remains a challenging task.

Acknowledgement

The research leading to these results has received funding from the European Union's Horizon 2020 research and innovation program, Marie Sklodowska-Curie Actions, under grant agreement no. 764979, project "ENABLE," "European Network for Alloys Behaviour Law Enhancement." The authors thanks the anonymous reviewers for their helpful comments, especially for drawing the attention on the importance of heat conduction.

Appendix A. General equations of thermodynamics

The energy balance (first law of thermodynamics) with respect to the current configuration is written in the local form:

$$\rho \dot{e} = \underset{\sim}{\boldsymbol{\sigma}} : \underset{\sim}{\boldsymbol{D}} + \mathcal{Q}, \tag{A.1}$$

with $\underset{\sim}{\boldsymbol{D}} = (\underset{\sim}{\boldsymbol{l}} + \underset{\sim}{\boldsymbol{l}}^T)/2$ as the strain rate tensor, e the internal energy per unit mass and $\mathcal{Q}$ the heat supply per unit volume and unit time, which results from an external heat source r and heat conduction $\underline{\boldsymbol{q}}$ such that

$$\mathcal{Q} = r - \operatorname{div} \underline{\boldsymbol{q}}\,. \tag{A.2}$$

The second law of thermodynamics in the form of the local dissipation rate inequality with respect to the current configuration can be written as

$$\rho \dot{\eta} + \operatorname{div} \frac{\underline{\boldsymbol{q}}}{T} - \frac{r}{T} \geq 0, \tag{A.3}$$

where η is the entropy per unit mass and T is the absolute temperature. The Helmholtz free energy density function is introduced as

$$\Psi := e - T\eta. \tag{A.4}$$

The Clausius-Duhem inequality is now expressed with respect to the reference configuration as

$$J \underset{\sim}{\boldsymbol{\sigma}} : \underset{\sim}{\boldsymbol{D}} - \rho_0 (\dot{\Psi} + \eta \dot{T}) - \underline{\boldsymbol{Q}} \cdot \frac{\nabla_X T}{T} \geq 0, \tag{A.5}$$

where $\underline{\boldsymbol{Q}}$ is the heat conduction with respect to the reference configuration and given by

$$\underline{\boldsymbol{Q}} = J^{the} \underset{\sim}{\boldsymbol{F}}^{-1} \cdot \underline{\boldsymbol{q}}\,, \tag{A.6}$$

and $\nabla_X T$ is the Lagrangian gradient of temperature.

Appendix B. Expression for the temperature evolution

The expression for the temperature evolution can be derived by assuming Helmholtz free energy function as in Eq. (24):

$$\begin{aligned} \rho_0 \eta = -\rho_0 \frac{\partial \Psi}{\partial T} &= -\frac{1}{2} \underset{\sim}{\boldsymbol{E}}^{the} : \frac{\partial \underset{\approx}{\boldsymbol{\Lambda}}}{\partial T} : \underset{\sim}{\boldsymbol{E}}^{the} + \rho_0 C_\varepsilon \log\left(\frac{T}{T_0}\right) - \rho_0 \frac{\partial C_\varepsilon}{\partial T} \left[(T - T_0) - T \log\left(\frac{T}{T_0}\right) \right] \\ &\quad + (T - T_0) \frac{\partial \underset{\sim}{\boldsymbol{P}}}{\partial T} : \underset{\sim}{\boldsymbol{E}}^{the} + \underset{\sim}{\boldsymbol{P}} : \underset{\sim}{\boldsymbol{E}}^{the} - \rho_0 \frac{\partial \Psi_\zeta}{\partial T}. \end{aligned} \tag{B.1}$$

Furthermore, the variation of entropy with respect to time is computed as

$$\begin{aligned} \rho_0 \dot{\eta} = &- \underset{\sim}{\boldsymbol{E}}^{the} : \frac{\partial \underset{\approx}{\boldsymbol{\Lambda}}}{\partial T} : \dot{\underset{\sim}{\boldsymbol{E}}}^{the} - \dot{T} \frac{1}{2} \underset{\sim}{\boldsymbol{E}}^{the} : \frac{\partial^2 \underset{\approx}{\boldsymbol{\Lambda}}}{\partial T^2} : \underset{\sim}{\boldsymbol{E}}^{the} + \rho_0 C_\varepsilon \dot{T} + \rho_0 \frac{\partial C_\varepsilon}{\partial T} \left[\log\left(\frac{T}{T_0}\right) \right] \dot{T} \\ &- \rho_0 \frac{\partial^2 C_\varepsilon}{\partial T^2} \left[(T - T_0) - T \log\left(\frac{T}{T_0}\right) \right] \dot{T} + \dot{T} \frac{\partial \underset{\sim}{\boldsymbol{P}}}{\partial T} : \underset{\sim}{\boldsymbol{E}}^{the} + \dot{T} (T - T_0) \frac{\partial^2 \underset{\sim}{\boldsymbol{P}}}{\partial T^2} : \underset{\sim}{\boldsymbol{E}}^{the} \\ &+ (T - T_0) \frac{\partial \underset{\sim}{\boldsymbol{P}}}{\partial T} : \dot{\underset{\sim}{\boldsymbol{E}}}^{the} + \dot{T} \frac{\partial \underset{\sim}{\boldsymbol{P}}}{\partial T} : \underset{\sim}{\boldsymbol{E}}^{the} + \underset{\sim}{\boldsymbol{P}} : \dot{\underset{\sim}{\boldsymbol{E}}}^{the} - \rho_0 \left(\frac{\partial^2 \Psi_\zeta}{\partial T^2} \dot{T} + \frac{\partial^2 \Psi_\zeta}{\partial T \partial \zeta} \dot{\zeta} \right). \end{aligned} \tag{B.2}$$

Then the right hand side of (37) becomes

$$\rho_0\left[\frac{\partial\Psi}{\partial\zeta}\dot{\zeta}+T\dot{\eta}\right]=\rho_0\frac{\partial\Psi}{\partial\zeta}\dot{\zeta}+T\Bigg[-\underset{\sim}{\boldsymbol{E}}^{the}:\frac{\partial\underset{\approx}{\boldsymbol{\Lambda}}}{\partial T}:\dot{\underset{\sim}{\boldsymbol{E}}}^{the}-\dot{T}\frac{1}{2}\underset{\sim}{\boldsymbol{E}}^{the}:\frac{\partial^2\underset{\approx}{\boldsymbol{\Lambda}}}{\partial T^2}:\underset{\sim}{\boldsymbol{E}}^{the}+\rho_0C_\varepsilon\dot{T}$$
$$+\rho_0\frac{\partial C_\varepsilon}{\partial T}\left[\log\left(\frac{T}{T_0}\right)\right]\dot{T}-\rho_0\frac{\partial^2C_\varepsilon}{\partial T^2}\left[(T-T_0)-T\,\log\left(\frac{T}{T_0}\right)\right]\dot{T}+\dot{T}\frac{\partial\underset{\sim}{\boldsymbol{P}}}{\partial T}:\underset{\sim}{\boldsymbol{E}}^{the}$$
$$+\dot{T}(T-T_0)\frac{\partial^2\underset{\sim}{\boldsymbol{P}}}{\partial T^2}:\underset{\sim}{\boldsymbol{E}}^{the}+(T-T_0)\frac{\partial\underset{\sim}{\boldsymbol{P}}}{\partial T}:\dot{\underset{\sim}{\boldsymbol{E}}}^{the}+\dot{T}\frac{\partial\underset{\sim}{\boldsymbol{P}}}{\partial T}:\dot{\underset{\sim}{\boldsymbol{E}}}^{the}+\underset{\sim}{\boldsymbol{P}}:\dot{\underset{\sim}{\boldsymbol{E}}}^{the}$$
$$-\rho_0\left(\frac{\partial^2\Psi_\zeta}{\partial T^2}\dot{T}+\frac{\partial^2\Psi_\zeta}{\partial T\partial\zeta}\dot{\zeta}\right)\Bigg],\tag{B.3}$$

Finally, the rate of temperature change is obtained by substituting previous equation into (37)

$$\dot{T}=\Bigg[\underset{\sim}{\boldsymbol{\Pi}}^M:\underset{\sim}{\boldsymbol{L}}^p+S\dot{\gamma}_{cum}-\operatorname{div}\underline{\boldsymbol{q}}+r-\rho_0\frac{\partial\Psi}{\partial\zeta}\dot{\zeta}-T\Bigg(-\underset{\sim}{\boldsymbol{E}}^{the}:\frac{\partial\underset{\approx}{\boldsymbol{\Lambda}}}{\partial T}:\dot{\underset{\sim}{\boldsymbol{E}}}^{the}+(T-T_0)\frac{\partial\underset{\sim}{\boldsymbol{P}}}{\partial T}:\dot{\underset{\sim}{\boldsymbol{E}}}^{th}$$
$$+\underset{\sim}{\boldsymbol{P}}:\dot{\underset{\sim}{\boldsymbol{E}}}^{the}-\rho_0\frac{\partial^2\Psi_\zeta}{\partial T\partial\zeta}\dot{\zeta}\Bigg)\Bigg]\Bigg[-T\frac{1}{2}\underset{\sim}{\boldsymbol{E}}^{the}:\frac{\partial^2\underset{\approx}{\boldsymbol{\Lambda}}}{\partial T^2}:\underset{\sim}{\boldsymbol{E}}^{the}+\rho_0C_\varepsilon+\rho_0\frac{\partial C_\varepsilon}{\partial T}\left[\log\left(\frac{T}{T_0}\right)\right]T$$
$$-\rho_0\frac{\partial^2C_\varepsilon}{\partial T^2}\left[(T-T_0)-T\,\log\left(\frac{T}{T_0}\right)\right]T+T\frac{\partial\underset{\sim}{\boldsymbol{P}}}{\partial T}:\underset{\sim}{\boldsymbol{E}}^{the}+T(T-T_0)\frac{\partial^2\underset{\sim}{\boldsymbol{P}}}{\partial T^2}:\underset{\sim}{\boldsymbol{E}}^{the}$$
$$+T\frac{\partial\underset{\sim}{\boldsymbol{P}}}{\partial T}:\underset{\sim}{\boldsymbol{E}}^{the}-\rho_0\frac{\partial^2\Psi_\zeta}{\partial T^2}T\Bigg]^{-1},\tag{B.4}$$

up to $T=T_{melt}$, where T_{melt} is the melting temperature of the material.

Appendix C. Analytical reference solution for linear strain softening

Consider a periodic strip made of a thick rectangular plate of width W along the $\underline{\boldsymbol{X}}_1$ direction, length L along the $\underline{\boldsymbol{X}}_2$ direction, and thickness T along the $\underline{\boldsymbol{X}}_3$ direction (Fig. C.28). It is made of a single crystal material possessing a single slip system under simple shear conditions. The slip direction $\underline{\boldsymbol{m}}$ and the normal to the slip plane $\underline{\boldsymbol{n}}$ are respectively parallel to $\underline{\boldsymbol{X}}_1$ and $\underline{\boldsymbol{X}}_2$. The strain rate sensitivity parameters n, K in Eq. (6) are chosen in such a way that the material response is almost rate-independent. A macroscopic deformation gradient $\bar{\underset{\sim}{\boldsymbol{F}}}$ is applied such that

$$\underline{\boldsymbol{u}}=(\bar{\underset{\sim}{\boldsymbol{F}}}-\underset{\sim}{\boldsymbol{1}})\cdot\underline{\boldsymbol{X}}+\underline{\boldsymbol{\nu}}(\underline{\boldsymbol{X}}),\quad\text{with}\quad\bar{\underset{\sim}{\boldsymbol{F}}}=\underset{\sim}{\boldsymbol{1}}+\bar{F}_{12}(\underline{\boldsymbol{m}}\otimes\underline{\boldsymbol{n}}),\tag{C.1}$$

where $\underline{\boldsymbol{\nu}}$ is a periodic fluctuation of the displacement. The origin O of the strip is constrained such that

$$\underline{\boldsymbol{u}}(X=0,Y=0,Z=0)=0.\tag{C.2}$$

It is assumed that elastic deformations remain small in the absence of lattice rotation in the considered slip configuration, i.e., $|F^e_{12}|\ll 1$ with

$$\underset{\sim}{\boldsymbol{F}}^e=\underset{\sim}{\boldsymbol{F}}\cdot\underset{\sim}{\boldsymbol{F}}^{p-1}=\underset{\sim}{\boldsymbol{1}}+F^e_{12}(\underline{\boldsymbol{m}}\otimes\underline{\boldsymbol{n}}),\tag{C.3}$$

and therefore, the elastic Green-Lagrange strain tensor can be expressed as follows:

$$\underset{\sim}{\boldsymbol{E}}^{the}\simeq\frac{F^e_{12}}{2}(\underline{\boldsymbol{m}}\otimes\underline{\boldsymbol{n}}+\underline{\boldsymbol{n}}\otimes\underline{\boldsymbol{m}}).\tag{C.4}$$

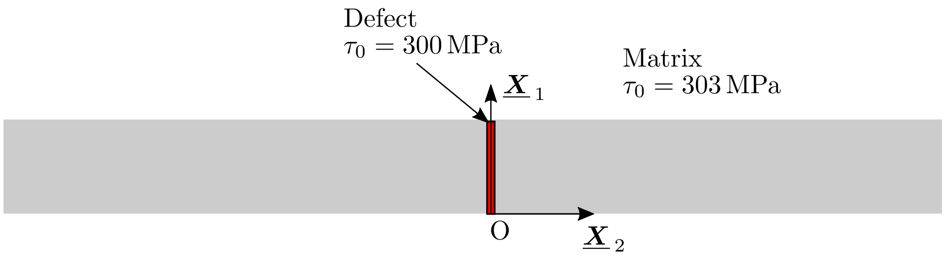

Fig. C.28: Single crystal trip with a central defect (red line).

where thermal expansion is set to zero in the present isothermal example. Moreover, the Piola stress $\underset{\sim}{\boldsymbol{\Pi}}^e$ in this instance is given by

$$\underset{\sim}{\boldsymbol{\Pi}}^e = \underset{\approx}{\boldsymbol{\Lambda}} : \underset{\sim}{\boldsymbol{E}}^{the} \simeq \Pi^e_{12}(\underline{\boldsymbol{m}} \otimes \underline{\boldsymbol{n}} + \underline{\boldsymbol{n}} \otimes \underline{\boldsymbol{m}}). \tag{C.5}$$

For small elastic deformations, the Piola and Mandel stresses coincide: $\underset{\sim}{\boldsymbol{\Pi}}^M \simeq \underset{\sim}{\boldsymbol{\Pi}}^e$. The resolved shear stress τ^r on the single slip system is given by

$$\tau = \underset{\sim}{\boldsymbol{\Pi}}^M : (\underline{\boldsymbol{m}} \otimes \underline{\boldsymbol{n}}). \tag{C.6}$$

Furthermore, equilibrium requires the shear stress component to be uniform which implies that the resolved shear stress τ is also invariant along $\underline{\boldsymbol{X}}_1$, $\underline{\boldsymbol{X}}_2$ and $\underline{\boldsymbol{X}}_3$.

The quasi-equality between the microslip variable γ_χ and the accumulated plastic strain γ is ensured by the coupling modulus H_χ. The yield condition including the linear strain softening can be written as follows:

$$f = |\tau| - (\tau_0 + H\gamma + H_\chi(\gamma - \gamma_\chi)) = 0 \quad \text{with} \quad H < 0. \tag{C.7}$$

A partial differential equation governing the microslip is given by

$$A\frac{\partial^2 \gamma_\chi}{\partial X_2^2} = H_\chi(\gamma_\chi - \gamma). \tag{C.8}$$

Substituting (C.7) for γ into (C.8) leads to another form of the partial differential equation

$$A\frac{\partial^2 \gamma_\chi}{\partial X_2^2} - \frac{HH_\chi}{H + H_\chi}\gamma_\chi + \frac{H_\chi}{H + H_\chi}(|\tau| - \tau_0) = 0. \tag{C.9}$$

In the case of linear strain softening, it can be shown that (C.9) takes the form

$$\frac{\partial^2 \gamma_\chi}{\partial X_2^2} - \left(\frac{2\pi}{\lambda}\right)^2 \gamma_\chi = -\left(\frac{2\pi}{\lambda}\right)^2 \kappa, \tag{C.10}$$

where λ is a characteristic length and κ a constant. They are defined as follows:

$$\lambda = 2\pi\sqrt{\frac{A(H + H_\chi)}{|H|H_\chi}}, \quad \kappa = \left(\frac{\lambda}{2\pi}\right)^2 \frac{H_\chi}{A(H + H_\chi)}(|\tau| - \tau_0). \tag{C.11}$$

The differential equation in (C.10) governing γ_χ is only valid in the region where plastic loading takes place which can be identified with the interval $X_2 \in [\frac{-\lambda}{2}, \frac{\lambda}{2}]$. This interval is the strain localization zone and outside elastic unloading takes place. The solution is of the form

$$\gamma_\chi(X_2) = a_1 \cos\left(2\pi\frac{X_2}{\lambda}\right) + a_2 \sin\left(2\pi\frac{X_2}{\lambda}\right) - \kappa. \tag{C.12}$$

where a_1, a_2 are integration constants. For symmetry reasons, $\gamma_\chi(X_2) = \gamma_\chi(-X_2)$ which requires that $a_2 = 0$. At the elastic/plastic interfaces, i.e at $X_2 = \pm\frac{\lambda}{2}$, continuity of microslip γ_χ and of the generalized stress normal to the interface $\underline{\boldsymbol{M}} \cdot \underline{\boldsymbol{X}}_2$ must hold, therefore

$$\gamma_\chi\left(\pm\frac{\lambda}{2}\right) \simeq \gamma\left(\pm\frac{\lambda}{2}\right) = 0, \tag{C.13}$$

$$\underline{\boldsymbol{M}}\left(\pm\frac{\lambda}{2}\right) \cdot \underline{\boldsymbol{X}}_2 = A\frac{d\gamma_\chi}{dX_2}\bigg|_{X_2=\pm\frac{\lambda}{2}} = 0. \tag{C.14}$$

In (C.13), we have assumed that the penalty parameter H_χ is high enough for γ_χ and γ almost to coincide, i.e. $e_p \simeq 0$. Combining (C.13) and (C.14) with (C.12) gives

$$a_1 = \frac{|\tau| - \tau_0}{H}. \tag{C.15}$$

Moreover, the resolved shear stress is expressed as

$$\tau = \Pi^e_{12} = 2C_{44}E^{the}_{12} = \frac{2C_{44}}{L}\int_{\frac{-L}{2}}^{\frac{L}{2}}\left(\frac{F_{12}-\gamma}{2}\right)dX_2, \tag{C.16}$$

with C_{44} being the elastic shear modulus. From the yield condition given in (C.7), γ can be replaced by $\frac{|\tau|-\tau_0+H_\chi\gamma_\chi}{H+H_\chi}$ in (C.16) and integration gives an expression for τ as a function of applied macroscopic shear $\bar{F}_{12}$:

$$\tau = \frac{\bar{F}_{12} + \frac{\tau_0}{Z_e}}{\frac{1}{C_{44}} + \frac{1}{Z_e}}, \quad \text{with} \quad \frac{1}{Z_e} = \frac{\lambda}{HL}. \tag{C.17}$$

References

Abdul-Aziz, A., Kalluri, S., 1991. Estimation of the engineering elastic constants of a directionally solidified superalloy for finite element structural analysis. Technical Report 187036. NASA.

Abu Al-Rub, R.K., Voyiadjis, G.Z., 2006. A physically based gradient plasticity theory. International Journal of Plasticity 22, 654 – 684. doi:`10.1016/j.ijplas.2005.04.010`.

Acharya, A., Beaudoin, A., 2000. Grain-size effect in viscoplastic polycrystals at moderate strains. Journal of the Mechanics and Physics of Solids 48, 2213 – 2230. doi:`10.1016/S0022-5096(00)00013-2`.

Ahad, F., Enakoutsa, K., Solanki, K., Bammann, D., 2014. Nonlocal modeling in high-velocity impact failure of 6061-t6 aluminum. International Journal of Plasticity 55, 108–132. doi:`10.1016/j.ijplas.2013.10.001`.

Aifantis, E.C., 1984. On the microstructural origin of certain inelastic models. Journal of Engineering Materials and Technology 106, 326–330. doi:`10.1115/1.3225725`.

Aifantis, E.C., 1987. The physics of plastic deformation. International Journal of Plasticity 3, 211 – 247. doi:10.1016/0749-6419(87)90021-0.

Aifantis, K., Willis, J., 2005. The role of interfaces in enhancing the yield strength of composites and polycrystals. Journal of the Mechanics and Physics of Solids 53, 1047 – 1070. doi:10.1016/j.jmps.2004.12.003.

Anand, L., Aslan, O., Chester, S.A., 2012. A large-deformation gradient theory for elastic–plastic materials: Strain softening and regularization of shear bands. International Journal of Plasticity 30-31, 116 – 143. doi:10.1016/j.ijplas.2011.10.002.

Anand, L., Kim, K., Shawki, T., 1987. Onset of shear localization in viscoplastic solids. Journal of the Mechanics and Physics of Solids 35, 407 – 429. doi:10.1016/0022-5096(87)90045-7.

Armstrong, R., 1961. On size effects in polycrystal plasticity. Journal of the Mechanics and Physics of Solids 9, 196 – 199. doi:10.1016/0022-5096(61)90018-7.

Asaro, R., Rice, J., 1977. Strain localization in ductile single crystals. Journal of the Mechanics and Physics of Solids 25, 309 – 338. doi:10.1016/0022-5096(77)90001-1.

Bachmann, F., Hielscher, R., Schaeben, H., 2010. Texture analysis with MTEX-Free and Open Source Software Toolbox. Solid State Phenomena 160, 63–68. doi:10.4028/www.scientific.net/SSP.160.63.

Bargmann, S., Ekh, M., Runesson, K., Svendsen, B., 2010. Modeling of polycrystals with gradient crystal plasticity: A comparison of strategies. Philosophical Magazine 90, 1263–1288. doi:10.1080/14786430903334332.

Batra, R., Chen, L., 2001. Effect of viscoplastic relations on the instability strain, shear band initiation strain, the strain corresponding to the minimum shear band spacing, and the band width in a thermoviscoplastic material. International Journal of Plasticity 17, 1465–1489.

Batra, R., Kim, C., 1991. Effect of thermal conductivity on the initiation, growth and bandwidth of adiabatic shear bands. International Journal of Engineering Science 29, 949 – 960. doi:10.1016/0020-7225(91)90168-3.

Batra, R., Kim, C., 1992. Analysis of shear banding in twelve materials. International Journal of Plasticity 8, 425 – 452. doi:10.1016/0749-6419(92)90058-K.

Baucom, J., Zikry, M., 1999. Perturbation analysis of high strain-rate shear localization in b.c.c. crystalline materials. Acta Mechanica 137, 109–129. doi:10.1007/BF01313148.

Benallal, A., 2008. A note on ill-posedness for rate-dependent problems and its relation to the rate-independent case. Computational Mechanics 42, 261 – 269. doi:10.1007/s00466-008-0252-8.

Bertram, A., 2003. Finite thermoplasticity based on isomorphisms. International Journal of Plasticity 19, 2027–2050. doi:10.1016/S0749-6419(03)00057-3.

Bertram, A., 2015. Finite gradient elasticity and plasticity: a constitutive thermodynamical framework. Continuum Mechanics and Thermodynamics 27. doi:10.1007/s00161-014-0387-0.

Bertram, A., Krawietz, A., 2012. On the introduction of thermoplasticity. Acta Mechanica 223, 2257–2268. doi:0.1007/s00707-012-0700-6.

Besson, J., Cailletaud, G., Chaboche, J., Forest, S., 2009. Non-linear mechanics of materials. volume 167. Springer Science & Business Media.

Borg, U., 2007. A strain gradient crystal plasticity analysis of grain size effects in polycrystals. European Journal of Mechanics - A/Solids 26, 313 – 324. doi:10.1016/j.euromechsol.2006.09.006.

de Borst, R., Sluys, L., Mühlhaus, H., Pamin, J., 1993. Fundamental issues in finite element analyses of localization of deformation. Engineering Computations 10, 99–121.

Burns, T., Davies, M., 2002. On repeated adiabatic shear band formation during high-speed machining. International Journal of Plasticity 18, 487–506. doi:10.1016/S0749-6419(01)00006-7.

Chambon, R., Caillerie, D., Hassan, N.E., 1998. One-dimensional localisation studied with a second grade model. European Journal of Mechanics - A/Solids 17, 637 – 656. doi:10.1016/S0997-7538(99)80026-6.

Chang, Y.W., Asaro, R.J., 1980. Lattice rotations and localized shearing in single crystals. Arch. Mech. 32, 369–388. doi:10.1016/S0191-8141(97)00016-3.

Cordero, N., Forest, S., Busso, E., Berbenni, S., Cherkaoui, M., 2012. Grain size effects on plastic strain and dislocation density tensor fields in metal polycrystals. Computational Materials Science 52, 7 – 13. doi:10.1016/j.commatsci.2011.02.043.

Cordero, N., Gaubert, A., Forest, S., Busso, E., Gallerneau, F., Kruch, S., 2010. Size effects in generalised continuum crystal plasticity for two-phase laminates. Journal of the Mechanics and Physics of Solids 58, 1963–1994.

DeMange, J.J., Prakash, V., Pereira, J., 2009. Effects of material microstructure on blunt projectile penetration of a nickel-based super alloy. International Journal of Impact Engineering 36, 1027 – 1043. doi:10.1016/j.ijimpeng.2009.01.007.

Dève, H.E., Asaro, R.J., 1989. The development of plastic failure modes in crystalline materials: Shear bands in FCC polycrystals. Metallurgical Transactions A 20, 579–593. doi:10.1007/BF02667576.

Dillamore, I.L., Roberts, J.G., Bush, A.C., 1979. Occurrence of shear bands in heavily rolled cubic metals. Metal Science 13, 73–77. doi:10.1179/msc.1979.13.2.73.

Dillard, T., Forest, S., Ienny, P., 2006. Micromorphic continuum modelling of the deformation and fracture behaviour of nickel foams. European Journal of Mechanics - A/Solids 25, 526–549. doi:10.1016/j.euromechsol.2005.11.006.

Dodd, B., Bai, Y., 2012. Preface, in: Dodd, B., Bai, Y. (Eds.), Adiabatic Shear Localization (Second Edition). second edition ed.. Elsevier, Oxford, p. ix. doi:10.1016/B978-0-08-097781-2.00015-0.

Duszek-Perzyna, M., Perzyna, P., 1996. Adiabatic shear band localization of inelastic single crystals in symmetric double-slip process. Archive of Applied Mechanics 66, 369–384. doi:10.1007/BF00803672.

Duszek-Perzyna, M.K., Perzyna, P., 1993. Adiabatic shear band localization in elastic-plastic single crystals. International Journal of Solids and Structures 30, 61 – 89. doi:10.1016/0020-7683(93)90132-Q.

Eringen, A.C., 1999. Microcontinuum field theories. Springer, New York.

Evers, L., Brekelmans, W., Geers, M., 2004. Scale dependent crystal plasticity framework with dislocation density and grain boundary effects. International Journal of Solids and Structures 41, 5209 – 5230. doi:10.1016/j.ijsolstr.2004.04.021.

Forest, S., 2009. Micromorphic approach for gradient elasticity, viscoplasticity, and damage. Journal of Engineering Mechanics 135. doi:10.1061/(ASCE)0733-9399(2009)135:3(117).

Forest, S., 2016. Nonlinear regularisation operators as derived from the micromorphic approach to gradient elasticity, viscoplasticity and damage. Proc. R. Soc. A 472, 20150755. doi:10.1098/rspa.2015.0755.

Forest, S., Lorentz, E., 2004. Localization phenomena and regularization methods, in: Besson, J. (Ed.), Local approach to fracture. Les presses de l'ecole des mines de paris. Ecole d'été "Mécanique de l'endommagement et approche locale de la rupture" (MEALOR), juillet 2004, pp. 311–371.

Forest, S., Sievert, R., 2003. Elastoviscoplastic constitutive frameworks for generalized continua. Acta Mechanica 160, 71–111.

Geuzaine, C., Remacle, J., 2009. Gmsh: A 3-d finite element mesh generator with built-in pre- and post-processing facilities. International Journal for Numerical Methods in Engineering 79, 1309–1331. doi:10.1002/nme.2579.

Gilman, J.J., 1994. Micromechanics of shear banding. Mechanics of Materials 17, 83 – 96. doi:10.1016/0167-6636(94)90051-5.

Gurtin, M.E., Needleman, A., 2005. Boundary conditions in small-deformation, single-crystal plasticity that account for the burgers vector. Journal of the Mechanics and Physics of Solids 53, 1–31. doi:10.1016/j.jmps.2004.06.006.

Hall, E.O., 1951. The deformation and ageing of mild steel: III discussion of results. Proceedings of the Physical Society. Section B 64, 747–753. doi:10.1088/0370-1301/64/9/303.

Harirêche, O., Loret, B., 1992. 3D dynamic strain-localization : shear band pattern transition in solids. European Journal of Mechanics A/Solids 11, 735–751.

Iturbe, A., Giraud, E., Hormaetxe, E., Garay, A., Germain, G., Ostolaza, K., Arrazola, P., 2017. Mechanical characterization and modelling of inconel 718 material behavior for machining process assessment. Materials Science and Engineering: A 682, 441 – 453. doi:10.1016/j.msea.2016.11.054.

Jin, T., Mourad, H.M., Bronkhorst, C.A., Livescu, V., 2018. Finite element formulation with embedded weak discontinuities for strain localization under dynamic conditions. Comput. Mech. 61, 3–18. doi:10.1007/s00466-017-1470-8.

Johansson, J., Persson, C., Lai, H., Colliander, M.H., 2016. Microstructural examination of shear localisation during high strain rate deformation of alloy 718. Materials Science and Engineering: A 662, 363 – 372. doi:10.1016/j.msea.2016.03.080.

Johansson, J., Persson, C., Testa, G., Ruggiero, A., Bonora, N., Colliander, M.H., 2017. Effect of microstructure on dynamic shear localisation in alloy 718. Mechanics of Materials 109, 88 – 100.

Kaiser, T., Menzel, A., 2019. An incompatibility tensor-based gradient plasticity formulation-Theory and numerics. Computer Methods in Applied Mechanics and Engineering 345, 671 – 700. doi:10.1016/j.cma.2018.11.013.

Kapoor, R., Nemat-Nasser, S., 1998. Determination of temperature rise during high strain rate deformation. Mechanics of Materials 27, 1–12. doi:10.1016/S0167-6636(97)00036-7.

Kuroda, M., Tvergaard, V., 2006. Studies of scale dependent crystal viscoplasticity models. Journal of the Mechanics and Physics of Solids 54, 1789 – 1810. doi:10.1016/j.jmps.2006.04.002.

Landau, P., Osovski, S., Venkert, A., Gartnerova, V., Rittel, D., 2016. The genesis of adiabatic shear bands. Scientific Reports 6. doi:10.1038/srep37226.

Lemonds, J., Needleman, A., 1986. An analysis of shear band development incorporating heat conduction. Mechanics of Materials 5, 363–373. doi:10.1016/0167-6636(86)90040-2.

Li, S., Liu, W.K., Qian, D., Guduru, P.R., Rosakis, A.J., 2001. Dynamic shear band propagation and micro-structure of adiabatic shear band. Computer Methods in Applied Mechanics and Engineering 191, 73–92. doi:10.1016/S0045-7825(01)00245-6.

Lieou, C.K., Mourad, H.M., Bronkhorst, C.A., 2019. Strain localization and dynamic recrystallization in polycrystalline metals: Thermodynamic theory and simulation framework. International Journal of Plasticity 119, 171 – 187. doi:10.1016/j.ijplas.2019.03.005.

Ling, C., Besson, J., Forest, S., Tanguy, B., Latourte, F., Bosso, E., 2016. An elastoviscoplastic model for porous single crystals at finite strains and its assessment based on unit cell simulations. International Journal of Plasticity 84, 58–87.

Ling, C., Forest, S., Besson, J., Tanguy, B., Latourte, F., 2018. A reduced micromorphic single crystal plasticity model at finite deformations. application to strain localization and void growth in ductile metals. International Journal of Solids and Structures 134, 43 – 69. doi:10.1016/j.ijsolstr.2017.10.013.

Lisiecki, L., Nelson, D., Asaro, R., 1982. Lattice rotations, necking and localized deformation in fcc single crystals. Scripta Metallurgica 16, 441 – 448. doi:10.1016/0036-9748(82)90169-7.

Liu, J., Suo, T., Zhou, F., Li, Y., 2019. Size effect on onset and subsequent evolution of adiabatic shear band: Theoretical and numerical analysis. Acta Mechanica Solida Sinica 33, 294–306. doi:10.1007/s10338-019-00152-0.

Longère, P., 2018. Respective/combined roles of thermal softening and dynamic recrystallization in adiabatic shear banding initiation. Mechanics of Materials 117, 81 – 90. doi:10.1016/j.mechmat.2017.10.003.

Loret, B., Prevost, J.H., 1990. Dynamic strain localization in elasto-(visco-)plastic solids, Part 1. General formulation and one-dimensional examples. Computer Methods in Applied Mechanics and Engineering 83, 247–273. doi:doi.org/10.1016/0045-7825(90)90073-U.

Marano, A., Gélébart, L., Forest, S., 2021. FFT-based simulations of slip and kink bands formation in 3D polycrystals: influence of strain gradient crystal plasticity. Journal of the Mechanics and Physics of Solids 149, 104295. doi:10.1016/j.jmps.2021.104295.

Mazière, M., Forest, S., 2015. Strain gradient plasticity modeling and finite element simulation of Lüders band formation and propagation. Continuum Mechanics and Thermodynamics 27, 83–104. doi:10.1007/s00161-013-0331-8.

Mcauliffe, C., Waisman, H., 2013. Mesh insensitive formulation for initiation and growth of shear bands using mixed finite elements. Computational Mechanics 51, 807–823. doi:10.1007/s00466-012-0765-z.

McVeigh, C., Liu, W.K., 2010. Multiresolution continuum modeling of micro-void assisted dynamic adiabatic shear band propagation. Journal of the Mechanics and Physics of Solids 58, 187–205. doi:10.1016/j.jmps.2009.10.006.

Medyanik, S.N., Liu, W.K., Li, S., 2007. On criteria for dynamic adiabatic shear band propagation. Journal of The Mechanics and Physics of Solids 55, 1439–1461. doi:10.1016/j.jmps.2006.12.006.

Menzel, A., Steinmann, P., 2000. On the continuum formulation of higher gradient plasticity for single and polycrystals. Journal of the Mechanics and Physics of Solids 48, 1777–1796. doi:10.1016/S0022-5096(99)00024-1.

Meyers, M., Xu, Y., Xue, Q., Pérez-Prado, M., McNelley, T., 2003. Microstructural evolution in adiabatic shear localization in stainless steel. Acta Materialia 51, 1307–1325. doi:10.1063/1.1483603.

Molinari, A., Clifton, R.J., 1987. Analytical Characterization of Shear Localization in Thermoviscoplastic Materials. Journal of Applied Mechanics 54, 806–812. doi:10.1115/1.3173121.

Molinari, A., Musquar, C., Sutter, G., 2002. Adiabatic shear banding in high speed machining of ti–6al–4v: experiments and modeling. International Journal of Plasticity 18, 443–459. doi:10.1016/S0749-6419(01)00003-1.

Mourad, H., Bronkhorst, C., Livescu, V., Plohr, J., Cerreta, E., 2017. Modeling and simulation framework for dynamic strain localization in elasto-viscoplastic metallic materials subject to large deformations. International Journal of Plasticity 88, 1–26. doi:10.1016/j.ijplas.2016.09.009.

Musienko, A., Cailletaud, G., Diard, O., 2004. Damage, opening and sliding of grain boundaries, in: Ahzi, S and Cherkaoui, M and Khaleel, MA and Zbib, HM and Zikry, MA and Lamatina, B (Ed.), IUTAM Symposium on Multiscale Modeling and Characterization of Elastic-Inelastic Behavior of Engineering Materials, Proceedings, Int Union Theoret & Appl Mech; Moroccan State Secretary Sci Res; Pacific NW Natl Lab; USA European Res Off; Univ Cadi Ayyad, FSSM; Univ Metz, UFR MIM; Univ Louis Pasteur Strasbourg. pp. 149–156. IUTAM Symposium on Multiscale Modeling and Characterization of Elastic-Inelastic Behavior of Engineering Materials, Marrakech, MOROCCO, OCT 20-25, 2002.

Méric, L., Poubanne, P., Cailletaud, G., 1991. Single Crystal Modeling for Structural Calculations: Part 2—Finite Element Implementation. Journal of Engineering Materials and Technology 113, 171–182. doi:10.1115/1.2903375.

Needleman, A., 1988. Material rate dependence and mesh sensitivity in localization problems. Computer Methods in Applied Mechanics and Engineering 67, 69 – 85. doi:10.1016/0045-7825(88)90069-2.

Nemat-Nasser, S., Isaacs, J.B., Liu, M., 1998. Microstructure of high-strain, high-strain-rate deformed tantalum. Acta Materialia 46, 1307–1325.

Osovski, S., Rittel, D., Venkert, A., 2013. The respective influence of microstructural and thermal softening on adiabatic shear localization. Mechanics of Materials 56, 11 – 22. doi:10.1016/j.mechmat.2012.09.008.

Pamin, J., 1994. Gradient-dependent plasticity in numerical simulation of localization phenomena. Ph.D. thesis. Technische Univ., Delft (Netherlands).

Peirs, J., Verleysen, P., Degrieck, J., 2008. The use of hat-shaped specimens for dynamic shear testing. Foundations of civil and environmental engineering 11, 97–111. doi:10.1016/j.ijimpeng.2009.08.002.

Perzyna, P., 2002. Thermodynamical theory of inelastic single crystals. Engineering Transactions 50, 107–164.

Perzyna, P., Korbel, K., 1996. Analysis of the influence of the substructure of a crystal on shear band localization phenomena of plastic deformation. Mechanics of Materials 24, 141 – 158. doi:10.1016/S0167-6636(96)00032-4.

Perzyna, P., Korbel, K., 1998. Analysis of the influence of various effects on criteria for adiabatic shear band localization in single crystals. Acta Mechanica 129, 31 – 62. doi:10.1007/BF01379649.

Petch, N.J., 1953. The cleavage strength of polycrystals. J. Iron Steel Inst. 174, 25–28.

Phalke, V., Kaiser, T., Scherer, J.M., Forest, S., 2021. Modeling size effects in microwire torsion: A comparison between a lagrange multiplier-based and a $\mathrm{CurlF}^{\mathrm{p}}$ gradient crystal plasticity model. accepted in European Journal of Mechanics A/Solids .

Quey, R., Dawson, P., Barbe, F., 2011. Large-scale 3D random polycrystals for the finite element method: Generation, meshing and remeshing. Computer Methods in Applied Mechanics and Engineering 200, 1729 – 1745. doi:10.1016/j.cma.2011.01.002.

Quey, R., Renversade, L., 2018. Optimal polyhedral description of 3D polycrystals: Method and application to statistical and synchrotron X-ray diffraction data. Computer Methods in Applied Mechanics and Engineering 330, 308 – 333. doi:10.1016/j.cma.2017.10.029.

Ristinmaa, M., Wallin, M., Ottosen, N., 2007. Thermodynamic format and heat generation of isotropic hardening plasticity. Acta Mechanica 194, 103–121. doi:10.1007/s00707-007-0448-6.

Rittel, D., Kidane, A., Alkhader, M., Venkert, A., Landau, P., Ravichandran, G., 2012. On the dynamically stored energy of cold work in pure single crystal and polycrystalline copper. Acta Materialia 60, 3719–3728. doi:10.1016/j.actamat.2012.03.029.

Russo, R., Forest, S., Mata, F., 2020. Thermomechanics of cosserat medium: Modeling adiabatic shear bands in metals. Continuum Mechanics and Thermodynamics doi:10.1007/s00161-020-00930-z.

Scherer, J., Besson, J., Forest, S., Hure, J., Tanguy, B., 2019. Strain gradient crystal plasticity with evolving length scale: Application to voided irradiated materials. European Journal of Mechanics-A/Solids 77, 103768. doi:10.1016/j.euromechsol.2019.04.003.

Scherer, J., Phalke, V., Besson, J., Forest, S., Hure, J., Tanguy, B., 2020. Lagrange multiplier based vs micromorphic gradient-enhanced rate-(in)dependent crystal plasticity modelling and simulation. Computer Methods in Applied Mechanics and Engineering 372, 113426. doi:10.1016/j.cma.2020.113426.

Shawki, T., Clifton, R., 1989. Shear band formation in thermal viscoplastic materials. Mechanics of Materials 8, 13–43. doi:10.1016/0167-6636(89)90003-3.

Simo, J., Miehe, C., 1992. Associative coupled thermoplasticity at finite strains: Formulation, numerical analysis and implementation. Computer Methods in Applied Mechanics and Engineering 98, 41 – 104. doi:10.1016/0045-7825(92)90170-O.

Song, W., Hu, M., Zhang, H., Jin, Y., 2018. Effects of different heat treatments on the dynamic shear response and shear localization in inconel 718 alloy. Materials Science and Engineering: A 725, 76–87. doi:10.1016/j.msea.2018.04.010.

Steinmann, P., Kergaßner, A., Landkammer, P., Zbib, H.M., 2019. A novel continuum approach to gradient plasticity based on the complementing concepts of dislocation and disequilibrium densities. Journal of the Mechanics and Physics of Solids 132, 103680. doi:10.1016/j.jmps.2019.103680.

Taylor, G.I., Quinney, H., 1934. The Latent Energy Remaining in a Metal after Cold Working. Proceedings of the Royal Society of London Series A 143, 307–326.

Tsagrakis, I., Aifantis, E.C., 2015. On the effect of strain gradient on adiabatic shear banding. Metallurgical and Materials Transactions A 46, 4459–4467. doi:10.1007/s11661-014-2586-5.

Vignjevic, R., Djordjevic, N., Vuyst, T.D., Gemkow, S., 2018. Modelling of strain softening materials based on equivalent damage force. Computer Methods in Applied Mechanics and Engineering 335, 52 – 68. doi:10.1016/j.cma.2018.01.049.

Voyiadjis, G.Z., Al-Rub, R.K.A., 2005. Gradient plasticity theory with a variable length scale parameter. International Journal of Solids and Structures 42, 3998 – 4029. doi:10.1016/j.ijsolstr.2004.12.010.

Wang, W., Sluys, L., de Borst, R., 1996. Interaction between material length scale and imperfection size for localisation phenomena in viscoplastic media. European Journal of Mechanics. A, Solids 15, 447–464.

Wcisło, B., Pamin, J., 2017a. Local and non-local thermomechanical modeling of elastic-plastic materials undergoing large strains. International Journal for Numerical Methods in Engineering 109, 102–124. doi:10.1002/nme.5280.

Wcisło, B., Pamin, J., 2017b. Local and non-local thermomechanical modeling of elastic-plastic materials undergoing large strains. International Journal for Numerical Methods in Engineering 109, 102–124.

Wcisło, B., Pamin, J., Kowalczyk-Gajewska, K., Menzel, A., 2018. Numerical analysis of ellipticity condition for large strain plasticity. AIP Conference Proceedings 1922, 140008. doi:10.1063/1.5019150.

Wulfinghoff, S., Bayerschen, E., Böhlke, T., 2013. A gradient plasticity grain boundary yield theory. International Journal of Plasticity 51, 33–46.

Wulfinghoff, S., Forest, S., Böhlke, T., 2015. Strain gradient plasticity modeling of the cyclic behavior of laminate microstructures. Journal of the Mechanics and Physics of Solids 79, 1–20. doi:10.1016/j.jmps.2015.02.008.

Xu, Y., Zhang, J., Bai, Y., 2008. Shear localization in dynamic deformation: Microstructural evolution. Metallurgical and Materials Transactions A 39, 811–843. doi:10.1007/s11661-007-9431-z.

Xue, Q., Gray, G., Henrie, B., Maloy, S., Chen, S., 2005. Influence of shock prestraining on the formation of shear localization in 304 stainless steel. Metallurgical and Materials Transactions A 36, 1471–1486. doi:10.1007/s11661-005-0239-4.

Yan, N., Li, Z., Xu, Y., Meyers, M.A., 2021. Shear localization in metallic materials at high strain rates. Progress in Materials Science 119, 100755. doi:10.1016/j.pmatsci.2020.100755.

Yang, Q., Stainier, L., Ortiz, M., 2006. A variational formulation of the coupled thermo-mechanical boundary-value problem for general dissipative solids. Journal of the Mechanics and Physics of Solids 54, 401 – 424. doi:10.1016/j.jmps.2005.08.010.

Zbib, H.M., Aifantis, E.C., 1988. On the structure and width of shear bands. Scripta Metallurgica 22, 703–708. doi:10.1016/S0036-9748(88)80186-8.

Zhang, Z., Eakins, D.E., Dunne, F.P., 2016. On the formation of adiabatic shear bands in textured hcp polycrystals. International Journal of Plasticity 79, 196 – 216. doi:10.1016/j.ijplas.2015.12.004.

Zhu, H., Zbib, H., Aifantis, E.C., 1995. On the role of strain gradients in adiabatic shear banding. Acta Mechanica 111, 111–124. doi:10.1007/BF01187731.